2014

Nanostructured Plasmonic Interferometers for Ultrasensitive Label-Free Biosensing

Yongkang Gao
Lehigh University

Nanostructured Plasmonic Interferometers for Ultrasensitive Label-Free Biosensing

by

Yongkang Gao

Presented to the Graduate and Research Committee

of Lehigh University

in Candidacy for the Degree of

Doctor of Philosophy

in

Electrical Engineering

Lehigh University

January, 2014

Approved and recommended for acceptance as a dissertation in partial fulfillment of the requirements for the degree of Doctor of Philosophy.

Date

Dr. Filbert Bartoli

Dissertation Director

Accepted Date

Committee Member:

Dr. Filbert Bartoli

(Chairman and Advisor)

Dr. Yujie Ding

Dr. Xuanhong Cheng

Dr. Daniel Ou-Yang

Acknowledgements

First and foremost, I would like to express my sincere gratitude to my advisor Prof. Filbert Bartoli for his support, guidance, encouragement, and inspiration in the last five years of my Ph.D. study. All the achievements presented in this doctoral dissertation would not have been possible without the support and contribution from him. His scientific vision, critical thinking, and creativity are remarkable. He helps me gradually mature from a student to a scientist. I feel truly lucky to be Prof. Bartoli's student and have benefited in every possible way that a student can benefit under his extreme support and guidance.

I would also like to thank my committee members, Prof. Xuanhong Cheng, Prof. Yujie Ding, and Prof. Daniel Ou-Yang, for their advices and collaboration in my Ph.D. study. The presented biosensor work is a beautiful interdisciplinary project that requires expertise in the fields of both nanophotonics and biomedical science. I cannot image I can accomplish this much if not with their expertise and advices throughout these years. I also want to specially thank Prof. Qiaoqiang Gan. He is not only my colleague but also a friend to me, who is always there to help me out with his knowledge and patience. I have learned so much from him about how to perform research and how to think, read, and write logically and rigorously. I also want to express my appreciation to the assistance from my group mate Beibei Zeng and Zheming Xin.

I want to thank all my Chinese friends at Lehigh: Jiayuan Wu, Bo Lin, Yang Yu, Dawei Yin, Siliang Liu, Xin Wen, Yunfei Li, Yile Ge, Ran Huang, Ning Ding, Yidan Xia, Guan Sun, Zhao Tang, and Yan Xu. Thank you all for the time we spent together which makes my life colorful. Special thanks to Bo and Yang for all of your support and I'm honored to have you as my friends. I want to thank Yong Zhao from Texas Tech Univ. for being my friend since the first year of my undergraduate study and listening to all my complaints during this job hunting process. I want to thank Sicong Liu and Gang Jin for being my best friends for the last ten years. I enjoy every video chat we had and look forward to the beer drinking when I visit Beijing.

I want to thank Lu Yuan for all your understanding and support.

Finally, I want to thank my parents for all the love they gave me. It is because of your endless support, love, and caring that I can turn my dream into reality. I want to dedicate this dissertation to my parents.

To my parents

Table of Contents

List of Tables

List of Figures

Abstract

Optical biosensors that utilize surface plasmon resonance (SPR) technique to analyze the biomolecular interactions have been extensively explored in the last two decades and have become the gold standard for label-free biosensing. These powerful sensing tools allow fast, highly-sensitive monitoring of the interaction between biomolecules in real time, without the need for laborious fluorescent labeling, and have found widely ranging applications from biomedical diagnostics and drug discovery, to environmental sensing and food safety monitoring. However, the prism-coupling SPR geometry is complex and bulky, and has severely limited the integration of this technique into low-cost portable biomedical devices for point-of-care diagnostics and personal healthcare applications. Also, the complex prism-coupling scheme prevents the use of high numerical aperture (NA) optics to increase the spatial resolution for multi-channel, high-throughput detection in SPR imaging mode.

This dissertation is focused on the design and fabrication of a promising new class of nanopatterned interferometric SPR sensors that integrate the strengths of miniaturized nanoplasmonic architectures with sensitive optical interferometry techniques to achieve bold advances in SPR biosensing. The nanosensor chips developed provide superior sensing performance comparable to conventional SPR systems, but employing a far simpler collinear optical transmission geometry, which largely facilitates system integration, miniaturization, and low-cost production. Moreover, the fabricated nanostructure-based SPR sensors feature a very small sensor footprint, allowing massive

multiplexing on a chip for high-throughput detection. The successful transformation of SPR technique from bulky prism-coupling setup into this low-cost compact plasmonic platform would have a far-reaching impact on point-of-care diagnostic tools and also lead to advances in high-throughput sensing applications in proteomics, immunology, drug discovery, and fundamental cell biology research.

Chapter 1

Introduction

1.1 Motivation

Biosensors, with the ability to analyze and quantify biomolecular interactions, are indispensable tools in life science research, drug discovery, medical diagnostics, food/safety monitoring, homeland security, and the battlefield [1-4]. Generally, there are two protocols for biosensing: fluorescent-based detection and label-free detection. While fluorescent-based detection is extreme sensitive, the labeling step imposes extra time and cost demands, and may also interfere with the function of target biomolecules [3]. In contrast, label-free detection has recently drawn more attention as it provides opportunity to detect biomolecules in their natural forms without labeling and also allows quantitative, real-time kinetic measurement of biomolecular interactions [3-5]. Among various label-free biosensing technologies, surface plasmon resonance (SPR) continues to dominate the field because of their demonstrated very high sensitivity and real time detection capability [4]. As shown in Fig. 1.1 [6], SPR instrumentation is by far the most widely deployed form of label-free biosensing and have an approximately 40% market share.

While SPR is the current gold standard for label-free biosensing, it suffers from two important limitations that need to be addressed. First, the commercially available SPR instruments typically employ Kretschmann-based prism-coupling setup, which is

complex and bulky, increasing the size and cost of SPR systems [7-9]. This has severely hindered the integration of SPR technique into low-cost portable devices for point-of-care diagnostics and personal healthcare applications. Second, the attenuated total reflection geometry and the prism-coupling setup prevent the use of high NA optics in SPR imaging for high-throughput detection. A high NA is desired in order to magnify the image and increase the number of CCD pixels illuminated by light from a given probe area, thereby improving the sensor signal-to-noise. [10-13]. As a result, these important limitations of current SPR systems strongly motivate the search for a new type of SPR platform that is more suitable for low-cost point-of-care applications and high-throughput SPR imaging operation.

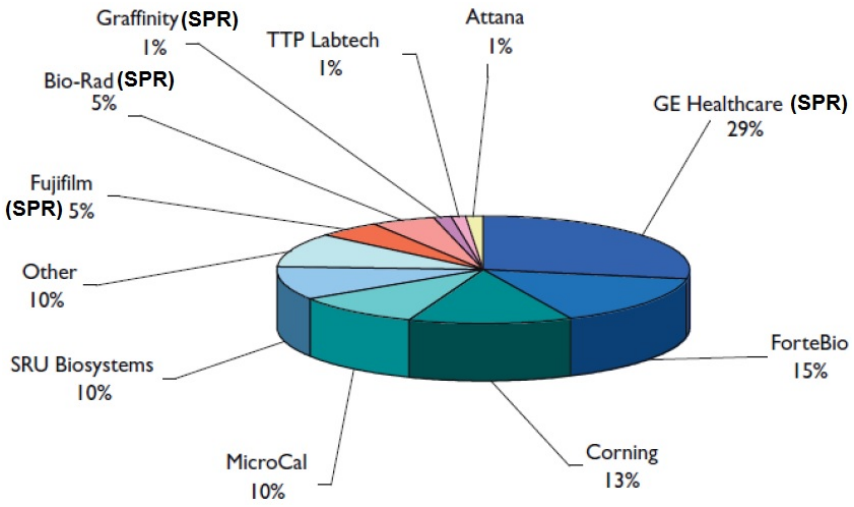

Fig. 1.1. Estimated vendor market share for label-free binding analysis instruments (2008 to 2010) [6].

Nanopatterned SPR (nanoplasmonic) biosensors, that employ nanopatterned hole arrays or nanoparticles to directly excite SPR in a simple collinear transmission

geometry, are a promising new generation of SPR sensors [14-19]. The simplicity of their optical transmission geometry offers substantial advantages for system integration and miniaturization. Moreover, these nanostructure-based sensors can have a footprint as small as a few square micrometers, allowing massive multiplexing on a sensor chip (10^7 sensors on a $1cm^2$ sensor area) for high-throughput sensing applications [10-13]. While promising, the performance of nanoplasmonic sensors reported to date is still not comparable to commercial SPR systems, which has severely limited the commercialization of this new sensing technique.

A significant focus of this dissertation will be the development of a novel class of nanoplasmonic interferometric sensors that integrated the strengths of nanoplasmonic structures (small footprint, simple optical geometry) with those of optical interferometry techniques (high sensitivity), to achieve bold advances in the performance of nanoplasmonic sensors. The results presented in this dissertation will enable the development of a new generation of nanopatterned SPR sensors with superior sensing sensitivity, simple compact optical configuration, and massive multiplexing capacity. A sensor with such sensing capabilities currently does not exist and will be essential to the development of low-cost, portable, point-of-care diagnostic devices and can lead to dramatic advances in various high-throughput sensing applications in proteomics, immunology, drug discovery, and fundamental cell biology research.

1.2 Surface Plasmon Resonance (SPR) systems

SPR sensors employ a special mode of electromagnetic field confined at a metal-dielectric interface - surface plasmon polaritons (SPPs) - to monitor the changes in the refractive index of the dielectric in the proximity of the interface [2-5]. SPPs are electromagnetic waves coupled to coherent charge oscillations at a metal-dielectric interface [16]. The dispersion relation of SPPs can be expressed as

$$k_{spp} = \frac{\omega}{c}\sqrt{\frac{n^2\varepsilon_m}{n^2+\varepsilon_m}}, \tag{1.1}$$

where ω is the angular frequency of the electromagnetic wave, c the speed of light in vacuum, ε_m the metal permittivity, and n is the refractive index of the medium covering the sensor surface. This dispersion condition can be satisfied for metals as the real part of ε_m is negative. Considering the complex permittivity of metal $\varepsilon_m = \varepsilon'_m + i\,\varepsilon''_m$, Eq. 1.1 can be rewritten as

$$k_{spp} = k'_{spp} + ik''_{spp} = \frac{\omega}{c}\sqrt{\frac{n^2\varepsilon'_m}{n^2+\varepsilon'_m}} + i\,\frac{\omega}{c}\frac{\varepsilon''_m}{2(\varepsilon'_m)^2}\left(\frac{n^2\varepsilon'_m}{n^2+\varepsilon'_m}\right)^{3/2}. \tag{1.2}$$

The real part of k_{spp} is shown by the solid curve in Fig. 1.2. For a frequency ω_0, there is a momentum mismatch between light and SPPs ($k_0 < k_{spp}$). As a result, this momentum mismatch must be bridged in order to couple free-space light into SPPs. We will discuss several popular SPP coupling techniques in section 1.2.1. The second consequence of this dispersion relation is that the wavevector of SPPs in the z direction k_z is imaginary, because $k_0 = k_{spp}^2 + k_z^2$ and $k_z^2 = k_0^2 - k_{spp}^2 < 0$. Accordingly, the field perpendicular to the surface decay exponentially with distance from the interface. Electromagnetic wave with this behavior is said to be evanescent (nonradiative), which prevents the power from

radiating away from the surface and results in confined optical field and associated strong light-matter interaction at the metal-dielectric interface for biosensing applications.

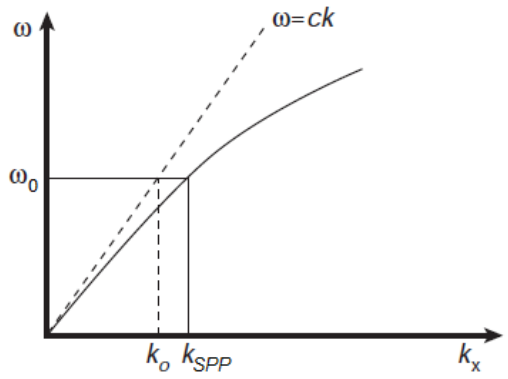

Fig. 1.2. The dispersion curve of SPPs, showing the momentum mismatch between light and SPPs.

There are several important characteristics of SPPs that need to be first defined. The propagation length of SPPs is defined as the propagation distance at which the intensity of SPPs decays by a factor of 1/*e* due to the absorption loss in the metal. As the SPP intensity decreases along the metal surface as exp (-2k_{spp}''x), the propagation length of SPPs can be calculated using

$$L_{spp} = \frac{1}{2k_{spp}''} = \frac{c}{w}\frac{(\varepsilon_m')^2}{\varepsilon_m''}\left(\frac{n^2+\varepsilon_m'}{n^2\varepsilon_m'}\right)^{3/2}. \quad (1.3)$$

SPPs also decay evanescently perpendicular to the dielectric-metal interface. The skin depth is then defined as the penetration depth into the dielectric and metal at which the SPP field falls to 1/*e*. The skin length of SPPs into the metal can be expressed as:

$$z_{metal} = \frac{\lambda}{2\pi}\left(\frac{|\varepsilon_m'+n^2|}{(\varepsilon_m')^2}\right)^{1/2}, \quad (1.4)$$

while the skin depth into the dielectric can be written as:

$$z_{dielectric} = \frac{\lambda}{2\pi}\left(\frac{|\varepsilon'_m + n^2|}{n^4}\right)^{1/2}. \quad (1.5)$$

1.2.1 Optical excitation of SPR

There are two important SPP coupling schemes that are commonly used in commercial SPR sensors: (1) prism coupling, (2) grating coupling. Prism SPP couplers represent the most frequently used method for optical excitation of SPPs. As shown in Fig. 1.3a, in the so-called Kretschmann prism-coupling configuration [4], the incident light is totally reflected at the prism-metal interface and generates an evanescent field penetrating into the metal layer. If the metal film is sufficiently thin (less than 100 nm in visible and near infrared part of spectrum [2]), the evanescent wave will resonantly couple with SPPs at the metal-dielectric interface. This coupling condition can be expressed as

$$\frac{\omega}{c} n_{prism} sin\theta = k_{spp} = \frac{\omega}{c}\sqrt{\frac{n^2 \varepsilon_m}{n^2 + \varepsilon_m}}, \quad (1.6)$$

where n_{prism} is the refractive index of the prism and θ is the incident angle. This coupling condition can be fulfilled for a specific θ and w, and the excitation of SPPs will be recognized as a minimum in the intensity of the reflected light. The usage of this resonant excitation condition for SPR sensing will be discussed in detail in the next section.

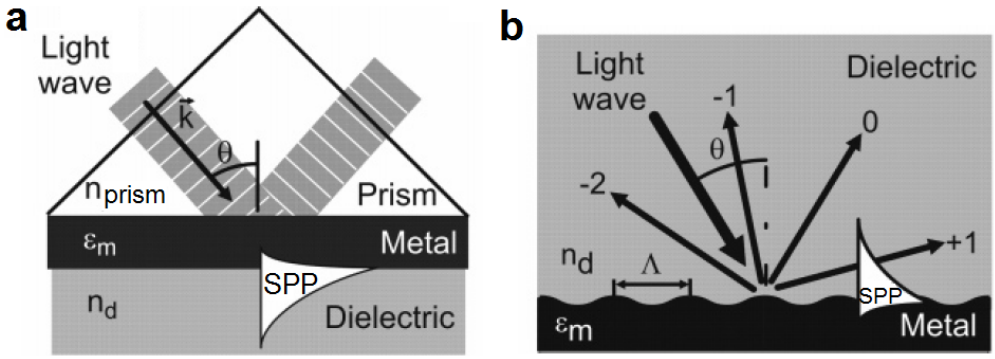

Fig. 1.3. SPP coupling through prism (a) and grating (b) [4].

The second commonly used coupling method is based on optical diffraction at a metallic grating structure. As shown in Fig. 1.3b, in this coupling method, a light wave is incident from the dielectric medium onto a metallic grating. If the momentum of the diffracted light parallel to the metal surface matches that of SPPs, the incident light will be coupled to SPPs. This process can be described as

$$\frac{\omega}{c} nsin\theta + m\frac{2\pi}{P} = \pm k_{spp}, \tag{1.7}$$

where m is an integer denoting the diffraction order and P is the period of the metallic grating.

1.2.2 SPR sensing using angular, wavelength, and intensity modulations

The optical setup of a typical commercial SPR system is illustrated in Fig. 1.4a, which consists of a light source, a prism SPP coupler, and a detector. The incident light excites SPPs through total internal reflection at the prism-dielectric interface when the momentum matching condition is fulfilled (Eq. 1.6). Depending on which modulation

approach is employed (angle, wavelength, or intensity), the detector records a minimum in the angle or wavelength spectrum, or the change in reflected light intensity at a fixed incident angle and wavelength. When there are biomolecules attached to the metal surface, the local refractive index increases, which produce a change in the propagation constant of the SPPs. This change in SPP propagation constant then alters the associated resonant coupling condition, which can be measured as the change in one of the characteristics of the light coupled to SPPs. Depending on which characteristics is measured, SPR sensors can be classified as angular, wavelength, or intensity modulated.

In SPR sensors using angular modulation, a narrow-band laser beam excites SPPs through the prism coupler and this resonant light-SPP coupling leads to a minimum in the angular spectrum of the sensor output. In SPR sensors based on wavelength modulation, the angle of the incident white light is kept constant, and the wavelength at which light is resonantly coupled to SPPs is measured as the sensor output. For SPR sensors using intensity modulation, the wavelength and the angle of the incident light are both kept constant, and the change in the intensity of the reflected light serves as the sensor output. Fig. 1.4b shows a typical SPR angular or wavelength spectrum, which features a reflection minimum at the resonant SPP coupling wavelength or angle. The increase of the refractive index Δn results in a red-shift of the spectrum ($\Delta\lambda$ or $\Delta\theta$) or a decrease in the reflected light intensity (ΔR) at the fixed wavelength or angle indicated by the dashed-dotted line.

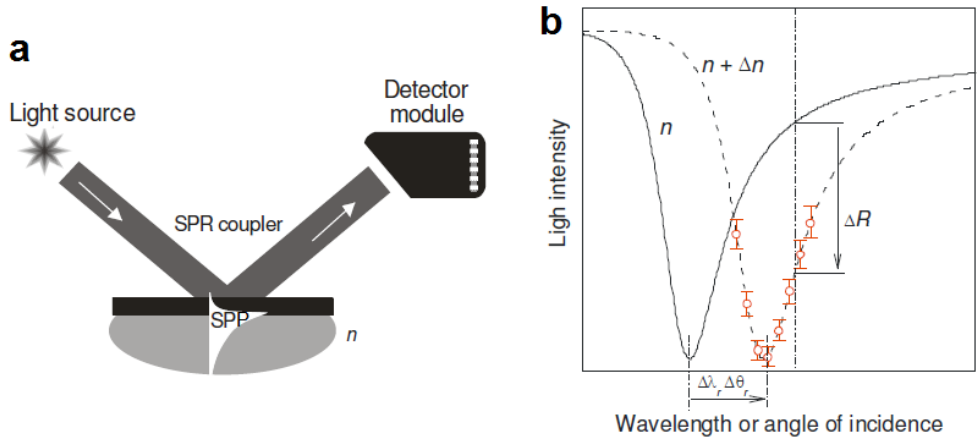

Fig. 1.4. (a) Schematic of an SPR sensor system. (b) Typical SPR wavelength or angular spectrum. The increase in the refractive index results in the red-shift of the angular spectrum (angular modulation), wavelength spectrum (wavelength modulation), or the decrease of the reflected light intensity ΔR (intensity modulation) [20].

While SPR has been demonstrated as a highly-sensitive technique for real-time label-free biomolecular detection, it is not conducive to sensor miniaturization and low-cost production, due to its optical complexity and bulky instrumentation. In order to overcome these limitations, new types of SPR platforms are required that use simple, compact, low-cost optical geometry design without compromising the sensing performance. In this dissertation, we will demonstrate a unique nanopatterned SPR platform that exhibits sensing performance similar to SPR systems but using significantly simpler collinear transmission optical setup, showing great promise for sensor miniaturization. Another significant challenge of current SPR systems is to extend the sensing capability to multiplexed assays for high-throughput applications in drug discovery, proteomics, and basic biology research, where thousands of biomolecular interactions need to be monitored simultaneously to significantly save on time and sample consumption [21]. SPR imaging (SPRi) is currently the most employed approach to address this need, which

typically employing a CCD camera to monitor the intensity distribution of light reflected from an SPR surface containing multiple sensing spots [21-23]. In the next section 1.2.3, SPRi technique will be discussed in detail, including their advantages and disadvantages and possible approaches to improve their performance.

1.2.3 SPR imaging for high-throughput sensing

SPRi technique combines the sensitivity of SPR with the spatial resolution of CCD imaging. It employs the intensity modulation method, as discussed in the last section, to measure the change in the reflected light intensity that occurs when the SPR spectrum red-shifts upon the biomolecular binding at the sensor surface. Fig. 1.5a shows a diagram of the SPRi setup [24], and Fig. 1.5b shows a typical CCD image captured by a SPR imager [25]. The light intensities reflected from the entire sensor surface can be monitored in real time and multiple biomolecular interactions can thus be analyzed simultaneously (up to several hundreds). These SPRi facilities have important impact in high-throughput sensing applications.

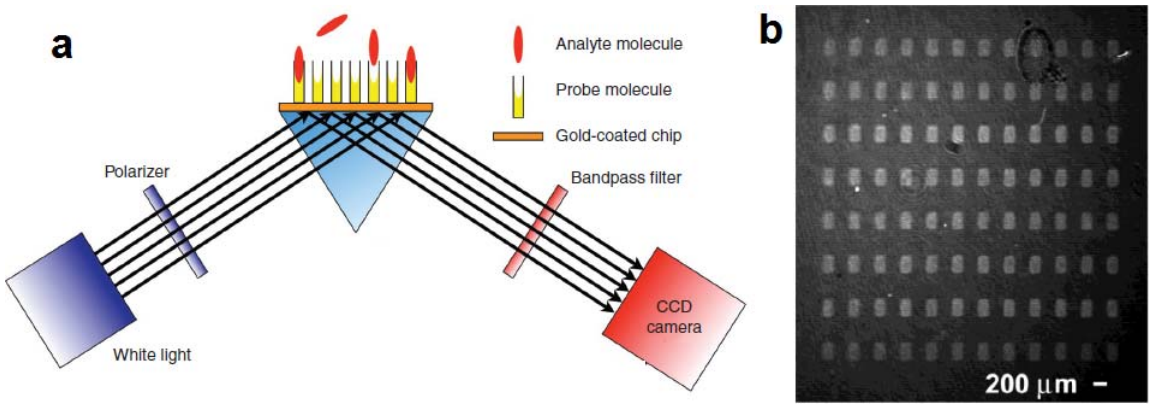

Fig. 1.5 (a) Diagram of the SPRi setup [24]. (b) A typical CCD image captured by a SPR imager. The bright regions correspond to sensing spots that were immobilized by receptor biomolecules [25].

While SPRi has been commercialized and successfully employed for a number of high-throughput applications, its sensing spot size is rather large (on the order of several hundred micrometers) [21], which has severely limited its throughput and the capability to probe nanovolumes and single cells. This is partially due to the prism-coupling scheme used in SPRi systems, which prevents the use of high NA optics. A high NA is desired in order to magnify the image and increase the number of CCD pixels illuminated by light for a given probe area, thereby improving the signal-to-noise [26]. The other factor that limits the spatial resolution of SPRi is the crosstalk from propagation of SPPs between adjacent sensing areas [10]. In order to improve the sensor signal-to-noise ratio and minimize SPP crosstalk, state-of-the-art commercial SPRi systems typically employ large sensing spots of 100 ~ 500 μm in diameter [21, 26-28]. This large sensing spot size is not suitable for probing nanovolumes and for single-cell analysis and has limited the number of sensing channels to several hundred for a 1 × 1 cm^2 sensor chip area.

In this dissertation, our first goal is the development of a nanopatterned interferometric SPR platform with performance comparable to commercial SPR platforms but using a much simpler optical geometry. The second goal is to scale up the developed platform for highly-multiplexed detection. Our developed sensor array has achieved a small sensing spot size of 100 μm^2, which is at least two order of magnitude smaller than that of commercial SPRi systems. More importantly, the developed sensor platform exhibits a sensing resolution comparable to that of SPRi instruments. This demonstrated sensor array can significantly increase the sensing throughput for numerous high-throughput applications and also opens opportunities to probe nanovolumes and for single-cell analysis.

1.2.4 Sensor performance characteristics

Resolution is a key sensor characteristic that is typically used to evaluate and compare the overall sensor performance. For bulk refractive index sensing, the resolution is defined as the smallest refractive index change that can produce a detectable signal in the sensor output. The unit of the sensor resolution is thus refractive index unit (RIU). The smallest detectable sensor output depends on the level of the uncertainty (noise) of the sensor output, which is related to the sensor system design (gold film thickness, surface roughness, incident light wavelength), the fluctuations in the intensity of the incident light, and also the electronic noise of the detector [2]. The SPR sensor noise can be easily characterized by measuring the time-resolved sensor output and determine the standard deviation of the sensor output (σ), i.e., signal-to-noise (SNR) of 1. For surface biomolecular sensing, the measure of resolution can be either the surface mass density of

the molecules (pg /mm^2) or biomolecule concentration in the sample solution (ng /ml). State-of-the-art commercial SPR systems typically employ angular modulation in a prism-coupling setup, and the sensor resolution can achieve 1×10^{-7} RIU in terms of bulk refractive index or 0.1 pg/mm^2 in terms of surface biomolecule mass density [4].

In SPRi system, another important sensor characteristic is the sensing spot size, which, as discussed above, directly determines the throughput of the device and the sensor probing volume. As the resolution of SPRi improves by integrating signal from a larger sensing spot size (spatial averaging), there is a trade-off between the sensor resolution and sensing spot size. Commercial SPRi systems typically employs a sensing spot size of 100 ~ 500 μm in diameter and exhibits a detection resolution of around 1×10^{-5} RIU [21, 26-28]. The reason for the lower resolution of SPRi comparing to SPR systems is that commercial SPR systems collect angular spectrums (a series of intensities) to determine the dip position, while SPRi measures only one intensity data at a fixed wavelength and angle, thus losing analytical data and typically exhibiting lower SNR than SPR systems [4].

1.3 Nanoplasmonic biosensors

The bulky optical instrumentation and difficulty in scaling up for high-throughput detection are two important limitations of current SPR systems. A new type of nanopatterned SPR (nanoplasmonic) sensors, that employ nanohole arrays or nanoparticles and operate in a simple collinear transmission geometry, has recently been proposed to address these two limitations. This new group of sensors is believed to be a promising alternative to the current prism-coupling SPR and SPRi systems [16-19] due to

their significantly simpler collinear transmission geometry, which offers promising opportunities for system miniaturization and low-cost production [19]. Through further integration on compact microfluidic platforms, nanoplasmonic biosensors hold great promise to develop fast, inexpensive, portable biomedical devices for point-of-care diagnostics and healthcare applications [9].

Besides the promise in device miniaturization and cost-effectiveness, another significant advantage of nanoplasmonic sensors is their capacity for massive multiplexing. Such nanostructure-based sensor arrays can have a sensor footprint as small as a few square micrometers and an on-chip packing density as high as 1×10^7 sensors per cm^2 [10]. Moreover, the simplicity of the optical transmission geometry allows the use of high NA optics to improve the imaging resolution for multiplexed detection in imaging mode. A system offering such a high multiplexing capacity would tremendously advance research in proteomics, drug discovery, diagnostics, and system biology.

So far, nanoplasmonic sensors based on extraordinary optical transmission (EOT) through nanohole arrays have been extensively studied for their potential use in high-throughput detection in imaging mode. This approach employs a CCD camera for the simultaneous measurement of the intensity variations of transmitted narrow-band light from multiple nanohole arrays, providing dynamic and multiplexed detection capability [10-13, 29-31]. However, the reported detection limits of EOT sensing platforms are typically in the 10^{-4} RIU range [10-12], which is one to two orders of magnitude poorer than that of commercial SPRi systems (see the upper left quadrant of Fig. 1.6) and is inadequate for many biomolecular sensing applications. As a result, the development of a

new nanoplasmonic sensor platform that combines the strength of nanopatterned SPR in sensing spot size and that of conventional SPR in mass detection resolution would have a far reaching impact on various high-throughput biosensing applications. These exciting possibilities are illustrated in the lower left quadrant of Fig. 1.6.

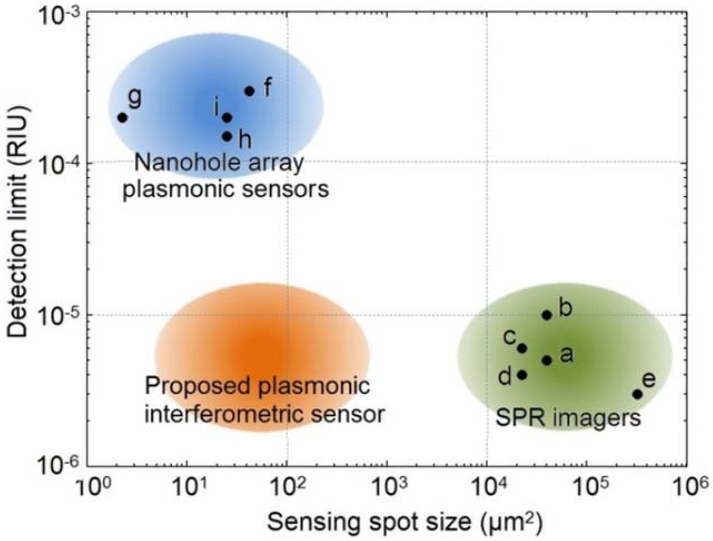

Fig. 1.6. Nanoplasmonic sensor platforms are typically limited by the sensing performance, while current SPRi systems limited by the multiplexing capacity. The proposed platform in this thesis provides both high sensing and multiplexing performance at the same time. The black dots indicate the reported experimental results in: (a) [21], (b) [26], (c) [27], (d) [28], (e) [32], (f) [29], (g) [31], (h) [11], and (i) [12].

1.3 Outline of the thesis

In this thesis, we will focus on the development of a novel class of nanoplasmonic interferometric sensors that integrate the strengths of nanoplasmonic architectures and those of optical interferometry techniques, to achieve both superior sensing performance and high multiplexing capability in a simple, low-cost, compact sensing platform. Such a sensor platform currently does not exist but will be essential for various high-throughput

sensing applications and facilitate the development of miniaturized portable biomedical devices for point-of-care diagnostics and personal healthcare applications.

Phase-sensitive interferometry is one of the most sensitive optical interrogation methods. Transforming this technique into nanoplasmonic platforms provides new exciting opportunities to significantly improve the sensor performance. In *Chapter 2*, we will first discuss the optical interferometry technique and the methods to combine interferometry with nanoplasmonic structure to realize novel plasmonic interferometers. In this chapter, we will also discuss the unique advantages of plasmonic interferometric sensors compared to previous plasmonic sensors based on EOT in nanohole arrays or localized plasmon resonance in nanoparticles.

In *Chapter 3*, we will discuss in detail the fabricated prototype plasmonic interferometric sensor device. In this dissertation, we have demonstrated, for the first time, the usage of a plasmonic interferometric sensor for highly-sensitive biomolecular detection. This novel sensor combines a Mach-Zehnder interferometer design and a simple two-nanoslit architecture with a 30 μm × 30 μm sensor footprint. It exhibits a sensor resolution of 7×10^{-6} RIU and a 10X better refractive index sensitivity than previous reported nanoplasmonic sensor platforms.

In *Chapter 4*, the developed nanoplasmonic interferometric sensor will be fabricated in a high-density array format to scale up the platform for high-throughput detection. A narrow-band light source and a CCD camera will be employed to perform the intensity

modulation in imaging mode and a novel self-referencing method will also be introduced to increase the sensitivity and reduce sensor noise for multiplexed detection.

A significant focus of the research presented in this thesis will be the design and optimization of novel plasmonic interferometer structures to achieve significant improvement in sensor performance. The results presented in *Chapter 3* and *4* demonstrate the promise of plamsonic interferometer for both single-channel spectral sensing and high-throughput detection in imaging mode. In *Chapter 5*, we will discuss the further optimization of the interferometer structure and systematically investigate the sensing and multiplexing performance of the optimized sensor platform. The results show that our developed sensor array can achieve a sensing spot size (10 μm × 10 μm) two order of magnitude smaller than commercial SPRi systems, but exhibiting a sensing resolution comparable to or better than that of SPRi instruments.

Providing a number of conceptual and scientific huddles can be overcome, the novel plasmonic multiplexed sensing platform developed in this dissertation would potentially lead to significant advances in point-of-care diagnostics and vast high-throughput array sensing applications in proteomics, diagnostics, drug screening, and fundamental cell biology research. *Chapter 6* will summarize the achievements of this dissertation and future research directions.

Chapter 2

SPP Interferometry

Existing nanoplasmonic sensors based on the resonant EOT effect in nanoaperture arrays or localized plasmon resonance in nanoparticles typically exhibit spectrally broad plasmon resonances due to the inevitable strong radiative and non-radiative losses in plasmonic resonant structures [17,19,33]. Such broad linewidths make it difficult to differentiate small spectrum shifts due to biomolecular bindings, posing significant obstacles to further improvements in sensor performance. In this thesis, we have proposed a fundamentally new approach that combines the concept of optical interferometry with plamsonic sensing, which opens up opportunities for a new class of nanoplasmonic sensor that can easily but significantly tune the plasmon line shape observed through SPP interference [34-36]. In this chapter, we will first discuss the basics of optical interferometry in section 2.1, and the methods to combine optical interferometry technique with plasmonic architecture to realize plasmonic interferometer devices in section 2.2. The usage of plamsonic interferometers for sensing applications and their unique advantages compared to existing plasmonic sensors will then be covered in section 2.3.

2.1 Basics of optical interferometry

Interferometry has long been a valuable tool for a variety of precision measurements using the interference phenomena produced by light waves [37]. Interferometric

measurements require an optical arrangement in which two or more light beams, derived from the same light source but traveling along separate paths, are made to combine and interfere. The resultant interference fringe is highly sensitive to the phase shift or the change in optical path length between the sample and reference arms. Thus, when the interference patterns are studied, the properties of the light waves and of the materials that they have traveled through can be explored. This technique, known as interferometry, has led to the development of some of the most sensitive optical interrogation methods and has found application in vast fields including astronomy, metrology, oceanography, and biological sciences [38].

If two light waves are to interfere to produce a stable interference fringe, the key requirement is that the light source must be coherent. The coherence effects can be divided into two classifications, temporal and spatial. Temporal coherence is a measure of the correlation between the light wave's phase at different times. Coherence time Δt is the time interval over which the phase of the light wave is still predicable, and the coherence length Δl defined as the distance the light wave travels in time Δt. The temporal coherence relates directly to the finite bandwidth Δv of the light source. If the light source is perfectly monochromatic, Δv would be zero and Δt and Δl infinite. Spatial coherence is a measure of the correlation between the light wave's phases at different points. It is related directly to the finite extent of the light source in space.

In order to achieve two separate, independent, adequately coherent light sources for interference, Thomas Young, in his classic double-slit experiment, brilliantly split a single wavefront from the same light source into two coherent portions, and then had

them superpose and interfere. In this experiment, as shown in Fig. 2.1 [39], a monochromatic light source illuminates a primary slit, which works as a spatial filter and produces spatially coherent beam. This light beam identically illuminates the closed placed two slits, which constitute two coherent secondary sources and generate constructive (bright band) and destructive (dark band) interference as the optical path difference between the two beams varies at different points on the screen.

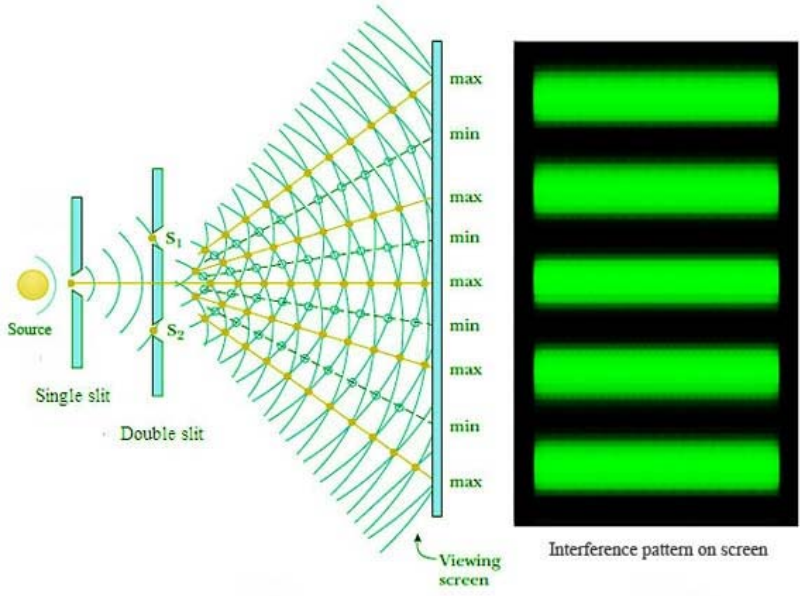

Fig. 2.1 Young's double slit experiment [39].

Besides this two-slit interferometer, other best known types of interferometers are Mach-Zehnder interferometer, Michelson interferometer, Fabry-Perot interferometer, and Sagnac interferometer. Interferometry technique has already been used in biological science as an analytical tool to monitor the interaction between biomolecules [38]. For example, Fig. 2.2 shows the schematic of a Mach-Zehnder interferometer (MZI), which

uses a silicon waveguiding method to monitor the difference in refractive index between the sensing and reference waveguides. Any biomolecular binding at the sensing arm produces a phase shift, which in turn leads to a change in the output intensity. State-of-the-art silicon MZI sensor can detection protein surface coverage as low as 0.25 pg/mm^2 [40], a resolution that compares favorably with commercial SPR sensors. However, the sensitivity of MZI device typically increases with the length of the arms. Sensitive MZI sensor typically utilizes sensing arms on the millimeter or centimeter scale, which requires large amount of sample solutions. The silicon waveguiding method is also not suitable for massive multiplexing detection due to the difficulty in coupling light into the micrometer scale waveguide. In fact, interferometry technique has also been combined with conventional SPR systems and produce sensor resolutions one order of magnitude better the current angular or wavelength-modulated SPR systems [41]. While this phase-sensitive SPR system demonstrates the promise of interferometry technique, the resulted SPR system still requires complex prism-coupling optical setup and is limited for high-throughput detection.

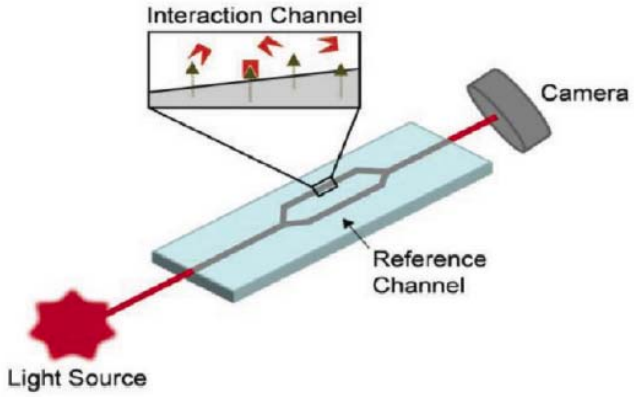

Fig. 2.2. Diagram of a silicon waveguide Mach-Zehnder interferometer [38].

2.2 SPP interferometry

So far, there are several works reported that have combined the concepts of interferometry with plamsonics in the so-called plasmonic interferometers [42-44]. As shown in Fig. 2.3, a plasmonic analogue of Thomas Young's double slit experiment was proposed and demonstrated. In this experiment, two nanoslits (200 nm wide) were patterned on a 200 nm thick gold film with a separation of 24.5 μm. When the whole structure is illuminated by a TM-polarized (the electric field perpendicular to the slits) collimated laser light (tunable from 740 to 830 nm), the transmission spectrum is seen to be approximately sinusoidally modulated as a function of the wavelength (dots in Fig. 2.3b). In contrast, there is no such modulation for a TE-polarized incident beam (the open squares). This observation can be explained using a model involving the propagation of SPPs between the two slits. When the light is TM-polarized, the SPPs excited at one slit propagates towards the other slit, where they will be partially back-converted into free-space light and interfere with the light that is directly transmitted through the slit [42]. The theoretical expression for the transmitted light intensity through the interferometer can be written as

$$I = 2\left[E_{light}^2 + E_{spp}^2 + 2\,E_{light}E_{spp}\cos\left(\frac{2\pi}{\lambda}n_{spp}d + \varphi_0\right)\right]. \qquad (2.1)$$

Here E_{spp} and E_{light} are the field amplitudes of SPP-mediated and directly-transmitted light components at one of the slits, respectively. d is the distance between the two slits. $n_{spp}(\lambda) = \mathrm{Re}((\varepsilon_m n^2/(\varepsilon_m + n^2))^{1/2})$ is the effective refractive index of SPPs propagating along

the metal surface between the two slits, and φ_0 is an additional phase shift associated with SPP excitation at the slits. The term $(2\pi d n_{spp}/\lambda + \varphi_0)$ represents the phase difference between the two interfering components, which varies with λ and thus leads to the observed constructive and destructive interferences.

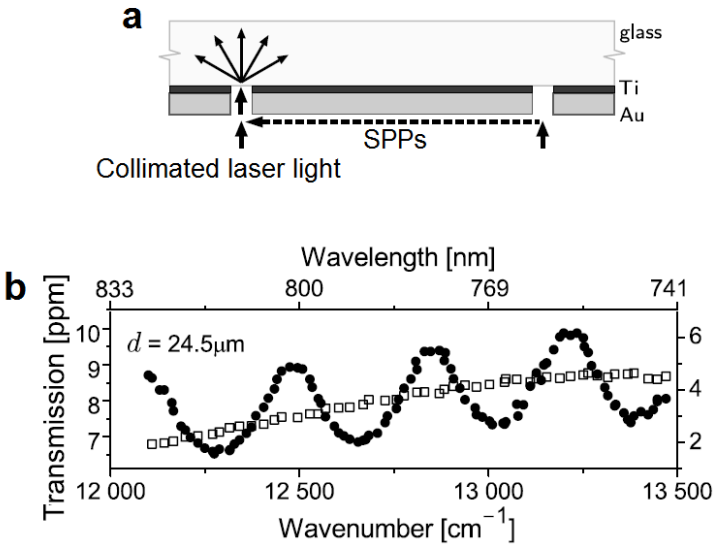

Fig. 2.3. (a) The schematic of the two-slit plasmonic interferometer. The dashed line indicates the excited SPPs. (b) The measured transmission spectrum for TM- (black dots) and TE- (open squares) polarized laser beam [42].

Another interesting plasmonic interferometer design is shown in Fig. 2.4a, which consists of a nanogroove-nanoslit structure. Our group has employed this interferometer structure to study the dependence of SPP coupling efficiency on the groove width [44]. While the details of this work are beyond the scope of this thesis, here we show some measured interference patterns to illustrate the working principle of this slit-groove pair as a plasmonic interferometer. Similar to the optical setup used in Fig. 2.3, when a TM-polarized collimated white light illuminates the interferometer structure, SPPs are excited

at the groove and propagate toward the slit, where they will be partially back-converted into free-space light and interfere with the light that directly transmits through the slit. As shown in Fig. 2.4b, the experimentally measured spectra (the upper frame) fit well with the theoretical predictions (the lower frame) calculated using Eq. 2.1, demonstrating the working principle of this plamsonic interferometer. Note that the interference period gradually decreases as *d* increases, which is in fact an interesting phenomenon that can be utilized to optimize the nanoplasmonic sensor performance. We will discuss in the next section the unique advantages of plamsonic interferometric sensors.

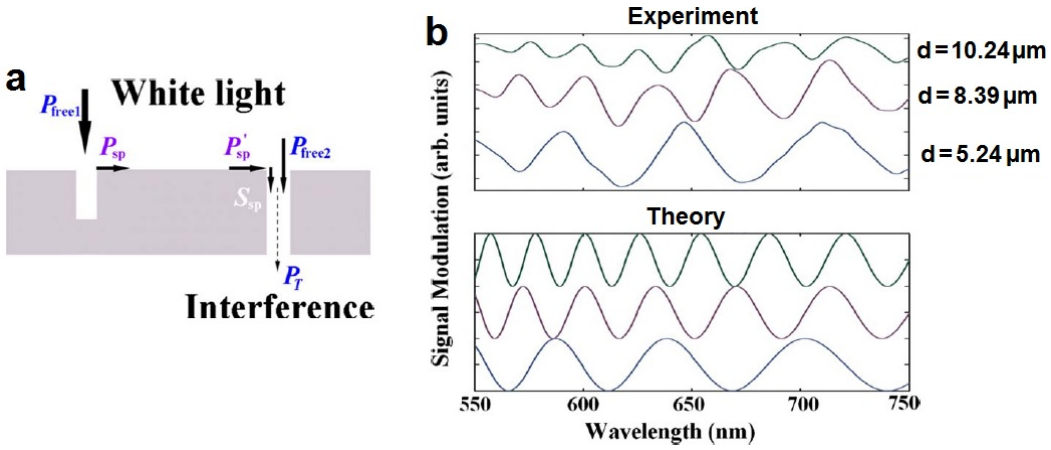

Fig. 2.4. (a) The schematic of the slit-groove plasmonic interferometer. (b) The experimentally measured and theoretical spectrum for interferometers with different slit-groove distance (5.24, 8.39, and 10.23 μm, from top to bottom).

2.3 Optical sensing suing SPP interferometry

Existing nanoplasmonic sensors based on localized plasmon resonance in nanoparticles or the resonant EOT effect in metal nanoaperture arrays typically exhibit broad peak linewidths because of strong radiative (scattering) and non-radiative (ohmic) losses

[17,19,33]. Such broad linewidths increase difficulties to differentiate small spectrum shifts due to biomolecular bindings. To optimize the performance of nanoplasmonic sensors, improvements in several basic plasmon characteristics are required: a very narrow spectral linewidth, a high spectral contrast, and a large spectral shift for modest changes in refractive index [18]. Consequently, plasmon line shape engineering is emerging as an important means to optimize the plasmonic sensor performance [45-48]. For example, the concepts of plasmonic Fano resonance and plasmon induced transparency have generated considerable interest due to their narrow linewidths associated with the subradiant dark modes [45-48]. Plasmon linewidths as small as 4 nm have been experimentally measured using these approaches [33]. However, these efforts suffer from the relatively low spectral contrast and weak resonance intensity of sub-radiant modes, which in fact greatly limit the overall sensor performance [33,47,49].

Different from existing nanoplamsonic sensors, plasmon sensing peaks are generated through spectral SPP interference in plamsonic interferometers, allowing flexible tailoring of the plasmon lineshapes through control of the amplitude and phase properties of SPPs [36]. For example, as shown in Fig. 2.4b, the linewidth of the interference peak can be effectively controlled by tuning the length of the interferometer arms (d), which alleviates the loss issues associated with previous resonant plasmonic nanostructures. Also, as will be shown in the following chapters, by appropriately designing the interferometer structure to balance the intensities of two interfering components, we can achieve interference patterns with very high spectral contrast, which is beneficial for optimized sensing. Moreover, the refractive index sensitivity can also be effectively

controlled. As will be discussed in Chapter 3, we have demonstrated a nanoplasmonic Mach-Zehnder interferometer with 10X higher sensitivity than previous reported nanoplamsonic sensors [34], showing great promise to significantly improve the sensor performance.

2.4 Summary

In summary, optical interferometry techniques are among the most sensitive optical interrogation methods. By combining the concepts of interferometry with plasmonics, we can develop plamsonic interferometric sensor with much greater flexibility, easy but significantly tuning of the plasmon line shape to achieve narrow interference linewidth, high spectral contrast, and high refractive index sensitivity, all key characteristics to achieve optimized plasmonic sensor performance. In the following chapters, we will discuss in detail several of our interferometric sensor designs and our demonstration of greatly improved performance compared to existing plasmonic sensor platforms.

Chapter 3

Plasmonic interferometers for highly-sensitive biosensing

In this chapter, we will introduce the design, fabrication, and characterization of our first prototype nanoplasmonic sensor device. To the best of our knowledge, this is the first time plasmonic interferometer was employed for ultrasensitive biomolecular sensing. We have fabricated a plasmonic Mach-Zehnder interferometer (MZI) integrated with a microfluidic chip to test the feasibility of the proposed sensing approach. The MZI is formed by patterning two parallel nanoslits in a thin metal film, and the sensor monitors the phase difference, induced by surface biomolecular adsorptions, between SPPs propagating on top and bottom surfaces of the metal film. The combination of a nanoplasmonic architecture and sensitive interferometric techniques in this compact sensing platform yields enhanced refractive index sensitivities greater than 3500 nm/RIU and record high sensing figures of merit exceeding 200 in the visible region, largely surpassing previous nanoplasmonic sensors and still holds potential for further improvement through optimization of the device structure. We also demonstrate real-time, label-free, quantitative monitoring of streptavidin-biotin specific binding with high signal-to-noise ratio in this simple, ultrasensitive, and miniaturized plasmonic biosensor.

3.1 Sensor design and fabrication

3.1.1 Detection principle

A schematic illustration of the plasmonic MZI is shown in Figure 3.1a. The device consists of a 350 nm-thick silver film evaporated onto a flat fused silica microscope slide. Focused ion beam (FIB) milling was used to fabricate a series of double-slit patterns, with slit separation distances of 22.7, 34.2, 45.6 and 57.6 μm. Each slit is 35 μm long and 0.1 μm wide. A scanning electron microscope (SEM) image of a slit pair with a slit separation distance of 22.7 μm is shown in Figure 3.1b. Optical measurements were performed using an Olympus X81 inverted microscope. A white light beam from a 100W Halogen lamp was focused onto the left slit A from the metalized side of the sample (see the lower inset of Figure 3.1b). Slit A scatters part of the incident radiation into SPP modes in both sensing and reference arms, located at the top metal surface and buried bottom metal/substrate interface, respectively. The SPP waves launched in these two arms propagate towards the right slit B, where they interfere with each other and modulate the far-field scattering. The SPP-mediated radiation from slit B was collected in transmission mode by an X40 microscope objective to measure the spectral interference patterns. For a specific wavelength, the intensity of the far-field transmission depends on the phase difference between the two SPP waves at the top sensing surface and bottom reference surface, which is modulated when biomolecules are adsorbed on the sensing metal surface. For broadband illumination, a spectral shift of the interference pattern is observed. Note that the sensing and reference arms of this plasmonic MZI are vertically aligned and separated by a 350 nm-thick thin silver film, enabling a compact footprint and dense array packing. The silver film also serves as a protection layer for the buried

reference arm, eliminating the need for additional cladding layer deposition and etching procedures as required for conventional planar silicon MZI. The simplicity, compactness, and ease-of-fabrication of this plasmonic sensing platform make it attractive for integration into practical, cost-effective sensing devices with potential high multiplexing capability.

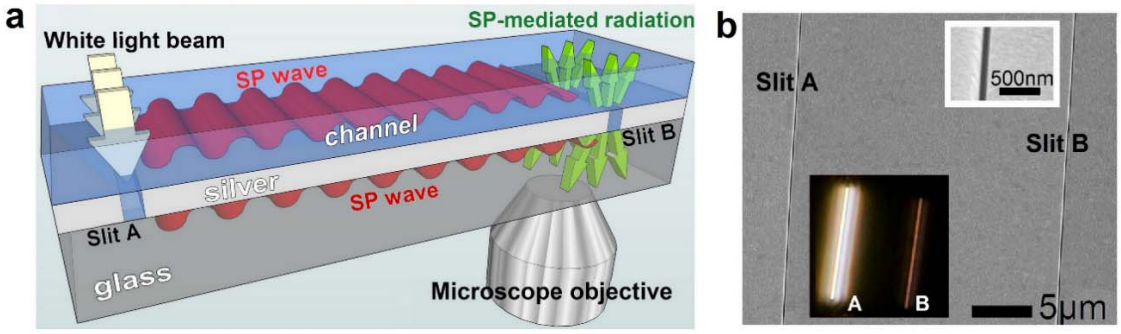

Fig. 3.1. (a) Schematic of the plasmonic MZI. (b) SEM image of a two-nanoslit structure (each slit being 35 μm long and 0.1 μm wide) with a slit separation of 22.7 μm. The upper inset shows a detailed SEM image of one nanoslit. The lower inset shows a transmission image of two-nanoslit structure with slit A being illuminated.

The solid curves in Figure 3.2 show the experimental spectra for a series of plasmonic MZIs in an air environment, with different slit separation distances *L*. The experiment was configured in a way that only SPP-mediated far-field scattering contributes to the resulting spectral oscillations (see section 3.1.2). Obvious interference patterns are observed as a function of wavelength under TM polarized illumination (with the electric field perpendicular to the long axis of the slit). For samples with larger *L*, the amplitudes of the interference oscillations are smaller, indicating increased SPP propagation loss at the metal surfaces. The decreased visibility of the interference is related to the increasing

intensity imbalance between the signals in two arms, as SPPs experience greater propagation loss at silver/glass interface. In this work, we focus on the spectral positions of the interference peaks and valleys and their usefulness for biosensing. To better interpret the measurements, theoretical interference patterns were calculated using the equation:

$$I \propto cos\left[\frac{2\pi L}{\lambda}(n_{spp1}(\lambda) - n_{spp2}(\lambda)) + \varphi_0\right]. \quad (3.1)$$

Here $n_{sppi}(\lambda) = \mathrm{Re}((\varepsilon_m(\lambda)n_i^2/\ (\varepsilon_m(\lambda) + n_i^2))^{1/2})$ is the effective refractive index of SPPs at the metal/dielectric interface, ε_m is the metal permittivity, n_i is the refractive index of the dielectric, and the subscript i = 1, 2 denote the upper dielectric and lower glass substrate, respectively. φ_0 is an additional constant phase shift. Using n_1 = 1.00 for air, the calculated interference patterns show a higher oscillation frequency than the experimental data, consistent with the results reported previously in ref. 44, 50 and 51. This discrepancy is attributed to formation of a contamination layer of Ag_2S (or a mixture of Ag_2O/AgO) on top of the silver surface [44, 50]. Here we assume a contamination film thickness of 4 nm (consistent with exposure in air for several-weeks [52]) and a film refractive index of 2.8 [53, 54], which yields an effective refractive index of the top dielectric n_1 = 1.03. One can see from Figure 3.2 that the resulting calculated oscillation frequencies and spectral positions of the peaks and valleys (dotted curves) agree very well with the measured data for plasmonic MZIs with four different L.

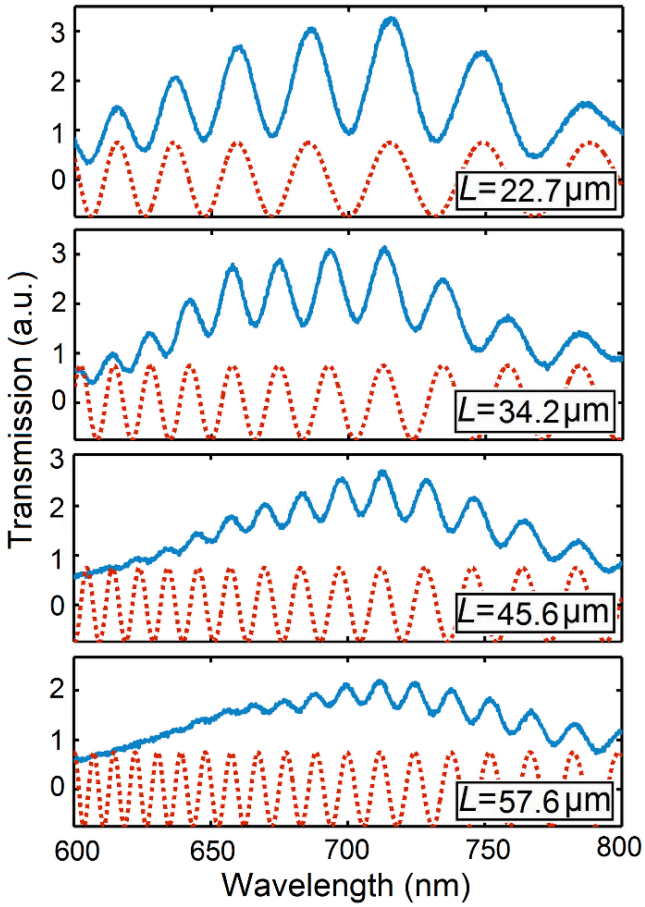

Fig. 3.2. Experimental SPP-mediated interference patterns for two-nanoslit structures in an air environment with slit separation distances, *L*, of 22.7, 34.2, 45.6, and 57.6 μm, respectively (from top to bottom). The upper spectra (solid curves) are experimental spectra and the lower dotted lines are theoretical predictions. No smoothing algorithm was applied to the experimental spectra.

3.1.2 Fabrication of the sensor chip and microfluidic channel

Fabrication of Plasmonic MZI. Silver films of 350nm thickness were deposited by e-beam evaporation (Indel system) onto flat fused silica microscope slides (Fisherbrand). Prior to the evaporation, the glass slides were cleaned thoroughly with acetone in an ultrasonic cleaner for 20min, followed by extensive DI water rinsing. Focused ion beam

(FIB) (FEI Dual-Beam system 235) milling (30kV, 30pA) was used to fabricate the double-slit plasmonic MZI structures.

Here FIB was used to fabricate the plasmonic MZI structures due to its convenience and precise control over nanostructure parameters, allowing us to test and optimize the interferometer design pretty easily. Fig. 3.3a shows several nanostructures we fabricated using FIB, showing the flexibility to easily and precisely control the nanostructure shape and geometrical parameters. For our long-term goal to do high-throughput biosensing, electron beam lithography will be employed for relatively large-area array patterning. Possibilities for low-cost sensor platforms will also be explored using other emerging relatively low-cost, large-area fabrication techniques such as nanoimprint lithography, colloidal lithography, or soft lithography.

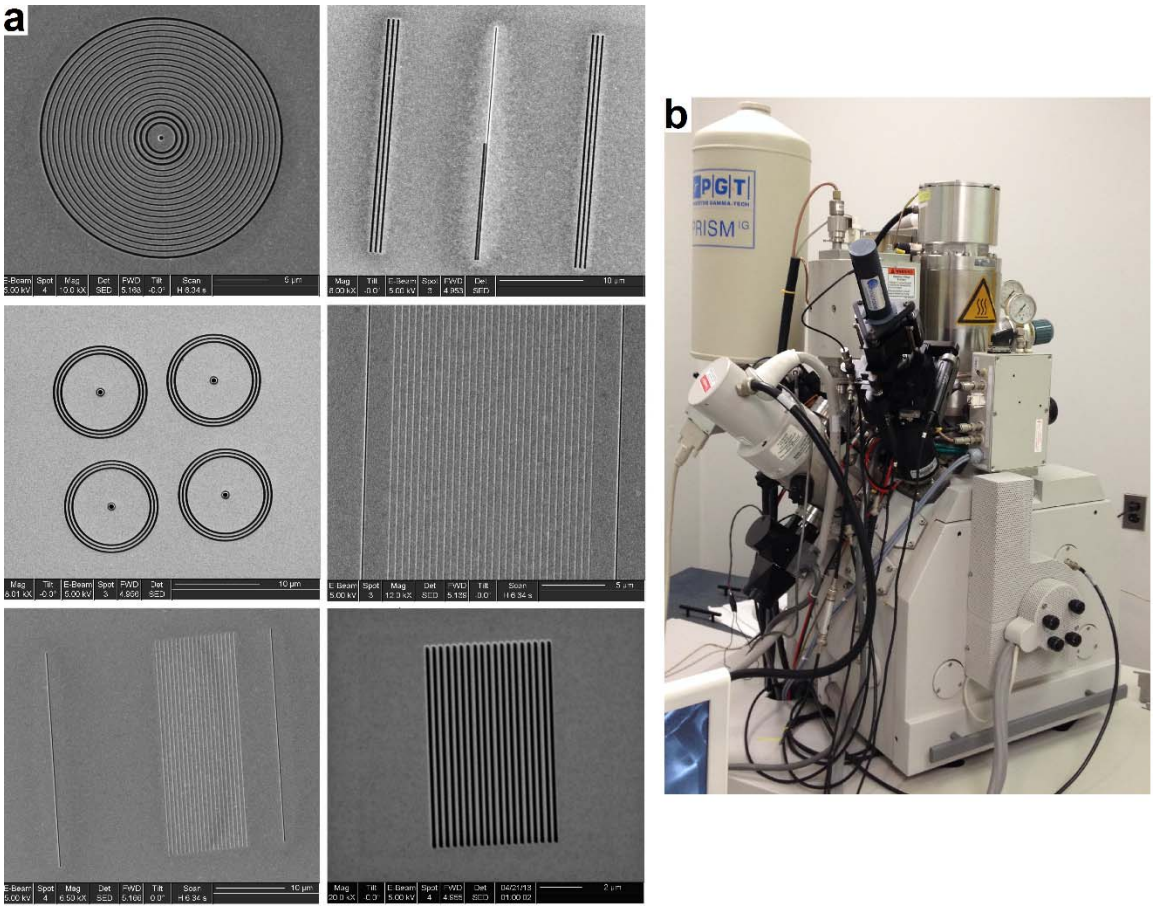

Fig. 3.3. (a) Various nanostructures fabricated using FIB. (b) FEI Dual-Beam system 235 used for the nanofabrication presented in this dissertation.

Fabrication of PDMS microfluidic channels. Microfluidic channels were fabricated by conventional photolithography. A SU-8 (SU8-50, Microchem) master mold of the channel (50 µm deep and 4 mm wide) was first patterned on a 3 inch wafer. A 10:1 ratio of PDMS (Sylgard 184, Dow corning) and curing agent were used to cast the mold, which was then baked at 70^{o}C for 3 h. The PDMS channel was cut and peeled from the master, and inlet and outlet holes were punched for tubing. The surfaces of the microfluidic channel and the nanopatterned sample were then activated by oxygen

plasma treatment (PX-250, March Instruments) and bonded to each other. Fig. 3.4a shows the fabricated PDMS microfluidic channel. A photograph of the fabricated plasmonic MZI sensor chip integrated with a microfludic chip is shown in Figure 3.4b.

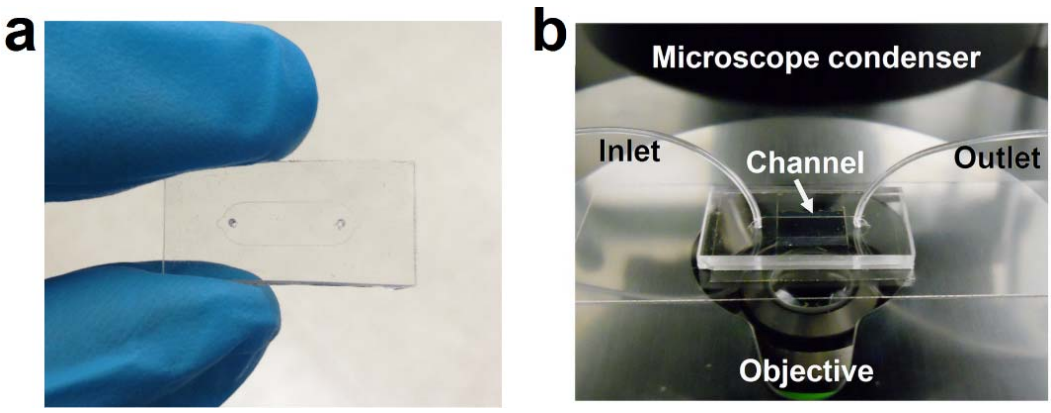

Fig. 3.4 (a) A photograph of the fabricated PDMS microfluidic channel. (b) A photograph of the fabricated sensor chip integrated with the microfluidic channel.

3.1.3 Experimental setup and optical measurement

A 100W halogen lamp was used to illuminate the double-slit patterns through the microscope condenser of an Olympus X81 inverted microscope. The condenser centering screws were tuned to move the image of the field diaphragm off the center of the viewing area, illuminating only the left slit A (with the right slit B located at the center of the viewing area). The transmitted light emanating from the slits was collected by an X40 microscope objective (NA = 0.6) and passed through an iris diaphragm that ensures only the SPP-mediated radiation from slit B in the center was transmitted. This signal was coupled into a multimode fiber bundle interfaced to a fiber-based compact spectrometer (Ocean Optics USB 4000). When slit A is illuminated and scattered light collected from

slit B, the SPP-mediated far-field scattering is directly observed. However, the measured data also contains a weak radiation leakage emanating directly from two open slits. Consequently, we designed another control experiment to remove the light leakage and to emphasize the SPP contribution. A CCD camera (Cooke sensicam qe) was employed to record the positions of the double slits. Under identical experimental conditions, a reference single slit was moved to the recorded positions of the left, and then the right slit of the interferometer. The collected transmission spectra were then both subtracted from the experimental raw data to yield the SPP-mediated far-field scattering spectra shown in Fig. 3.2. Each spectrum shown in this work represents an average of 100 acquisitions with an integration time of 100 ms for each acquisition.

3.2 Characterization of the sensor performance

3.2.1 Sensitivity calibration

The spectral interrogation sensitivity of the plasmonic MZI can be derived from Eq. 3.1 by setting the term $[n_{spp1}(\lambda) - n_{spp2}(\lambda)]/\lambda$ to be constant, yielding:

$$S = \left|\frac{\Delta\lambda}{\Delta n}\right| \approx \lambda\left(\frac{n_{spp1}(\lambda)}{n_1}\right)^3 \Bigg/ \left[\Delta n_{spp21}(\lambda) - \lambda\frac{d\Delta n_{spp21}}{d\lambda}\right] \tag{3.2}$$

where $\Delta n_{spp21}(\lambda) = n_{spp2}(\lambda) - n_{spp1}(\lambda)$. The bulk sensitivity, S, depends directly on the operational wavelength, the dielectric properties of the metal, and the refractive indices of the dielectrics at the upper and lower interfaces. For a liquid environment (n_1 = 1.330, n_2 = 1.516), this equation predicts S is greater than 3000 nm/RIU in the visible region. This sensitivity level is significantly higher than previously reported nanoplasmonic sensors

[17-19]. To confirm this theoretical prediction experimentally, a double-slit structure with L = 34.2 μm was fabricated and integrated with a PDMS microfludic channel (see Fig. 3.4b). To calibrate the sensitivity of plasmonic MZI, glycerol-water solutions were prepared with glycerol volume concentrations varying from 0.5 % to 3 %. An ellipsometer (J. A. Woollam, V-VASE) was used to measure their refractive indices, which range from n = 1.3302 to n = 1.3344. Glycerol-water solutions of varying glycerol concentration were then injected to tune the refractive indices of the liquid. As shown in Fig. 3.5a, the interference pattern blue-shifts as the liquid refractive index increases, in good agreement with the theoretical predictions (lower dotted curves). The peak and valley positions of the interference patterns around 700 nm and 730 nm (indicated by the upper and lower arrows, respectively) were measured as a function of the liquid refractive index and are plotted in Figure 3.5b. One can see that the positions of the peaks and the valleys vary approximately linearly with the refractive index of the liquid. The sensitivities are estimated to be 3524 nm/RIU (peak) and 3600 nm/RIU (valley) from the linear fits to the experimental data, in agreement with the theoretical predictions obtained using Eq. 3.2 (3448 nm/RIU and 3545 nm/RIU at 700 nm and 730 nm, respectively). These measured sensitivities are one order of magnitude larger than those reported previously for nanoplasmonic sensors based on nanoparticles [17-19], metamaterials [45], and EOT through nanoaperture arrays [55-57] in this visible spectral region. In addition, the unique plasmonic interferometry scheme allows broadband coupling of light into SPPs for biosensing. The availability of multiple interference maxima and minima enable this plasmonic MZI sensor to operate at different wavelengths where the SPP penetration

depth into the liquid environment may vary, permitting the detection of species with different size or/and absorption properties in a single device. With SPP fields extending different distances into the liquid, surface and solution refractive index changes may also be distinguished in a single measurement and at a single sensing spot, well-suited for applications in which solution index and compositions are poorly known.

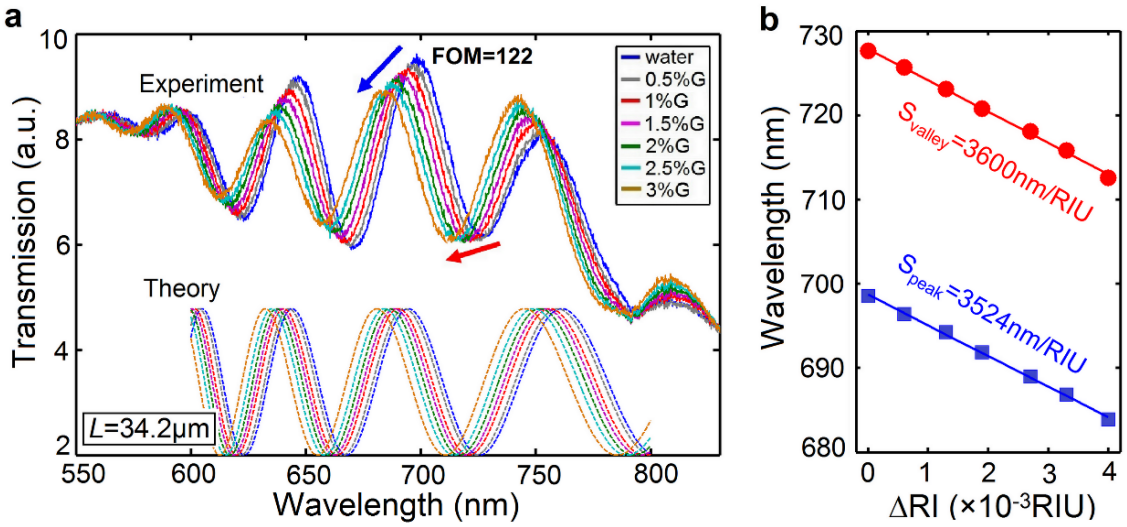

Fig. 3.5. (a) Measured spectra (upper curves) and calculated interference patterns (lower dotted curves) of plasmonic MZI with L = 34.2μm for water and glycerol-water solutions with six different glycerol volume concentrations (from 0.5 % to 3 %). The directions of the upper and lower arrows indicate the blue-shifts of the peak and the valley. No smoothing algorithm was applied. (b) Spectral position of the interference peak (squares) and valley (dots) versus refractive index of the solutions. The solid lines are linear fits to the data.

3.2.2 Figure of merit characterization

Eq 3.2 predicts that the sensor sensitivity can be increased further if n_{spp1} and n_{spp2} are closer in value. This can be realized by matching the refractive indices of the substrate and the top dielectric material. By setting the substrate refractive index n_2 = 1.38 (e.g.

using magnesium fluoride as the substrate), a sensitivity of more than 10000 nm/RIU is potentially achievable at a wavelength of 700 nm in a water environment ($n_1 = 1.33$). This would greatly surpass the performance of previous plasmonic sensors and compare favorably with conventional prism-based SPR sensors. However, it should be noted that when the two terms are closer in value the oscillation period of the interference pattern also increases, as described by the following expression:

$$P \approx \lambda^2 \Big/ L\left[\Delta n_{spp21}(\lambda) - \lambda \frac{d\Delta n_{spp21}}{d\lambda}\right] \tag{3.3}$$

When $n_{\text{spp1}} \approx n_{\text{spp2}}$, broadening in the interference pattern makes it difficult to resolve very small wavelength shifts of the peak or valley. To evaluate the performance of plasmonic sensors more precisely, researchers introduced the figure of merit FOM = $(\Delta\lambda/\Delta n)/\delta\lambda$ that simultaneously considers the refractive index sensitivity and the sharpness of the SPP resonance [58, 59]. Here $\Delta\lambda/\Delta n$ is the wavelength-shift sensitivity and $\delta\lambda$ is the full-width at half-maximum (FWHM) of the sensing peak. The FOM of our plasmonic MZI (for L = 34.2 μm) is found experimentally to be 122 (3524 nm/RIU /29 nm) for the interference peak (indicated by the upper arrow in Fig. 3.5a). This FOM value is among the highest reported for plasmonic biosensors in the visible region [33]. Moreover, the FOM for this plasmonic MZI can be increased further by properly choosing the operational wavelength and slit separation distance L. By letting the interference fringe width $\delta\lambda$ be equal to half of the oscillation period P, one can easily derive the FOM of plasmonic MZI from Eq. 3.2 and 3.3:

$$FOM = \frac{S}{\delta\lambda} = \frac{2S}{P} \approx \frac{2L}{\lambda}\left(\frac{n_{spp1}(\lambda)}{n_1}\right)^3 \tag{3.4}$$

Using Eq. 3.4, one can estimate the sensor FOM for our plasmonic MZI at L = 34.2 μm to be 113, which is in reasonable agreement with the experimentally derived value. Fig. 3.6a also shows the calculated FOM as a function of wavelength for different L. The results suggest that the value of FOM would increase further for shorter λ or larger L.

To demonstrate this theoretical prediction, plasmonic MZIs with L = 45.6 μm and 57.6 μm were fabricated and integrated with microfluidic channels. As shown in Fig. 3.6b, the linewidth of the interference peaks (see the arrows in Fig. 3.5a) decreases with increasing L for the plasmonic MZI in a water environment, consistent with predictions based on Eq. 3.3. Liquids with varying refractive index were then injected into the channel and the peak positions were extracted and plotted in Fig. 3.6c as a function of the liquid refractive index. For plasmonic MZIs with L = 45.6 μm and 57.6 μm, the measured sensitivities are 3470 nm/RIU and 3695 nm/RIU, respectively, and the resulting FOMs are 150 and 193, respectively, all in agreement with the theoretical calculations (see Table 1). The achieved FOM of 193 exceeds all reported FOM of previous non-prism-based plasmonic sensors in the visible region: the FOM is approximately 23 for sensors based on EOT in nanohole arrays [56], 14.5 for silver nanowell array based sensors [60], typically < 10 for localized-SP resonance sensors based on nanoparticles [17-19], 3.8 for metamaterial-based sensor [45], and 162 for high optical-quality nanohole array sensors using subradiant dark modes [33]. Our experimental FOM also surpasses the theoretically estimated FOM value of ≈ 108 for conventional prism-based SPR sensors [33, 61]. While

further FOM improvements are still possible for plasmonic MZI with larger L, the higher propagation loss of SPPs results in a decreased modulation depth and lower signal-to-noise ratio, limiting the further enhancement of the overall sensor performance for practical applications. This limitation could potentially be alleviated through several methods. First, the use of ultra-smooth metal films reported recently could decrease the scattering loss of propagating SPPs and enhance the sensor signal-to-noise ratio [62-64]. Second, slit dimensions can be optimized [44] to enhance the coupling from light to SPPs at the nanoslit.

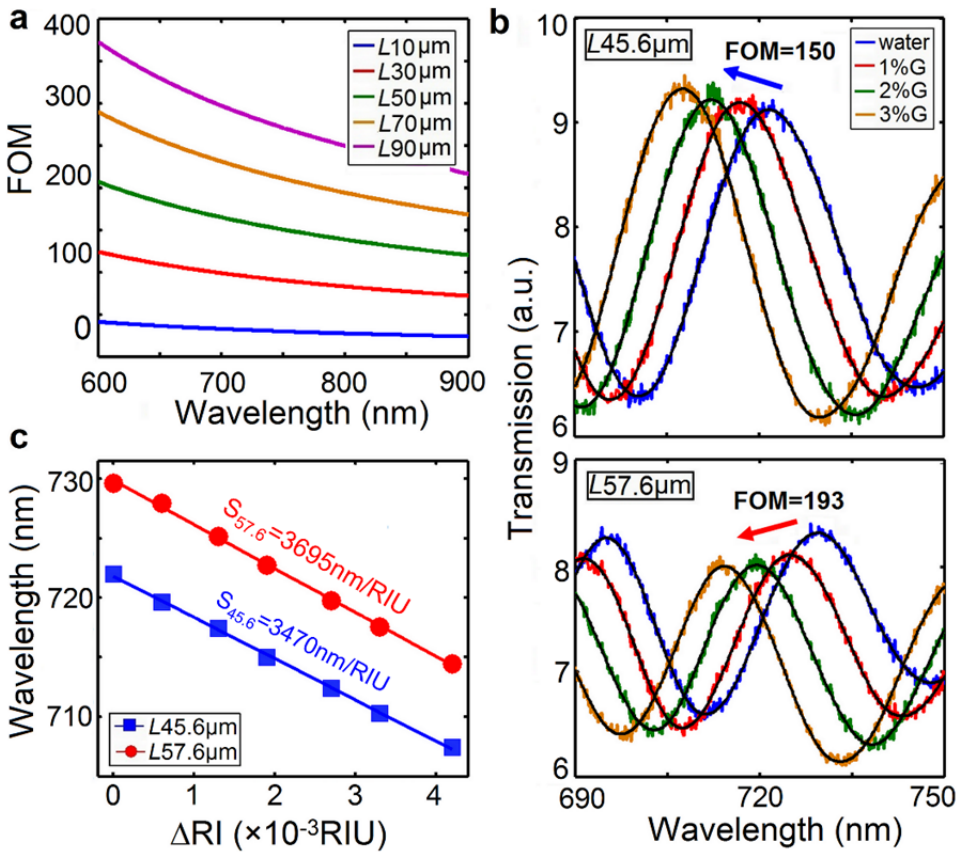

Fig. 3.6. (a) Calculated FOM of the plasmonic MZI as a function of wavelength for values of L ranging from 10 μm to 90 μm. (b) Measured spectra for glycerol-water solutions with varying glycerol volume concentrations. For clarity, only the spectra of

water and 1 %, 2 %, and 3 % glycerol-water solutions were shown. The black curves imposed on the experimental spectra are guides to the eye, obtained using a Fast Fourier Transform technique to filter out the high frequency noise of the raw data. Results are shown for L= 45.6 μm and 57.6 μm. (c) Spectral positions of the interference peak versus refractive index of the solution. Sensitivities are obtained using a linear fit to the experimental data.

L (μm)	Peak λ (nm)	Sensitivity (nm/RIU)	Linewidth (nm)	FOM
34.2	698	3524	29.0	122
		3442	30.4	113
45.6	722	3470	23.1	150
		3520	24.4	144
57.6	730	3695	19.1	193
		3545	19.7	180
69.0	734	3688	16.5	224
		3558	16.7	213

Table 1. Experimental and calculated sensor sensitivities, peak linewidths, and FOMs for plasmonic MZIs with different L (shaded areas show the theoretically calculated values).

3.3 Label-free, real-time biomolecular sensing

To examine the feasibility of this plasmonic MZI platform for real-time label-free biosensing, we employ the streptavidin-biotin affinity binding model. Measurements were performed using the same plasmonic MZI (L = 34.2 μm) discussed above in the bulk sensitivity calibration experiments. A 10 mM HEPES buffer (Sigma-Aldrich) was prepared and adjusted to pH 7.4. HEPES buffer was first injected into the microfluidic channel using a syringe pump (Harvard Apparatus) at a flow rate of 20 μL/min and run

for 20 min to define the baseline of the experiment. 500 μg/ml biotinylated BSA (Thermal Scientific) was then injected and run for 20 min to functionalize the sensor surface with a monolayer of bBSA. We then focused on the interference peak around 690 nm and recorded its spectral position in real-time using a Lorentzian peak fitting method. As shown by the lower data points in Fig. 3.7, the injection of a 300 nM (16 μg/ml) streptavidin (SA) solution generated a large peak shift of 15.7 nm. A subsequent buffer rinsing had little effect on the peak wavelength. To rule out nonspecific binding of the analyte, a control experiment was also performed, in which a 300 nM SA solution was injected into a reference channel, whose sensor surface was covered by a monolayer of BSA without biotin conjugation. This was followed by a buffer rinse. A very small blue-shift of the peak (0.7 nm) is observed (see the upper data points in Fig. 3.7), possibly due to nonspecific binding events. The net peak shift of 15 nm is therefore associated with the specific binding of biotin and SA. This value is considerably larger than previously reported results (*e.g.,* 3.8 nm for 370 nM SA in gold nanodot arrays [65], 6 nm for 370 nM SA in nanoparticle arrays [66], 3.5 - 4 nm for 5 μM SA in gold nanohole arrays [67] and 2 - 4 nm for 2 μM SA in a single gold nanoparticle platform [68]).

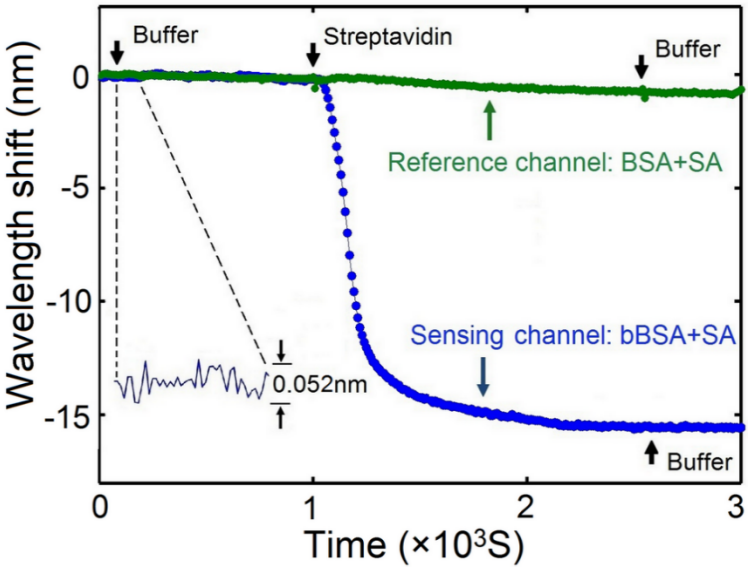

Fig. 3.7. The real-time sensor response upon the adsorption of molecules for biotin-SA sensing experiment (sensing channel) and BSA-SA experiment (reference channel). The inset shows the peak wavelength fluctuations in biotin-SA sensing experiment, which corresponds to an inherent noise level of 0.052 nm of the sensing system.

Next, we quantitatively extract the effective protein layer thickness d_e for streptavidin from the peak wavelength shift $\Delta\lambda$ using the simple expression [69]:

$$\Delta\lambda = S(n_l - n_b)(1 - e^{-\frac{2d_e}{l_d}}), \tag{3.5}$$

where S is the bulk sensitivity determined from the calibration experiment (S = 3524 nm/RIU), and n_l and n_b are the refractive indices of the adsorbed protein layer and buffer solution, respectively. l_d is the decay length of SPPs into the solution, which is calculated to be 310 nm at 690 nm. If one assumes the effective refractive index of protein is n = 1.5, the wavelength shift of 15 nm upon adsorption of SA protein layer corresponds to a calculated effective thickness of 3.9 nm for the SA layer, which agrees with the literature values for a SA monolayer [57, 70].

The fluctuations in the sensor response determine the noise level of our biosensor system. As shown in the lower inset of Fig. 3.7, an inherent noise of 0.026 nm (S/N = 1) was obtained. This system noise corresponds to a sensor resolution of 7.5×10^{-6} RIU [0.026 nm / (3524 nm/RIU)] and a high signal-to-noise ratio of 288 for monolayer SA binding. It is worth mentioning that no temperature control was employed in these experiments. Temperature fluctuations of around 0.1 K in water would be expected to cause a refractive index change of $\sim 1 \times 10^{-5}$ RIU [71]. Further improvement in sensor resolution and signal-to-noise ratio would be expected by optimizing the device structure, developing advanced data analysis methods, and using temperature control and lower-noise light source and detection systems.

3.4 Summary

In conclusion, we experimentally demonstrate a plasmonic MZI for miniaturized and ultrasensitive optical biosensing. The combination of sensitive interferometric techniques with nanoplasmonic architectures yields greatly enhanced sensitivities and record high FOM in a simple and compact sensor platform. The feasibility of this plasmonic interferometer for real-time, label-free, quantitative biosensing was also demonstrated by monitoring of protein binding events using simple transmission spectroscopy, significantly decreasing the sensing system complexity compared to conventional SPR measurements. The demonstrated enhanced sensor performance makes this miniaturized device promising for practical integrated biosensing devices for point-of-care diagnostics and healthcare applications.

Note that while this first-generation prototype nanosensor device has superior sensing performance and a compact footprint, its multiplexing capacity is somewhat limited due to its non-collinear transmission geometry (slit A needs to be illuminated while scattered light collected from slit B). Also, the spectral modulation method that was employed is not suitable for dynamic, highly multiplexed biosensing. As a result, the application of this demonstrated sensing device is limited for single-channel biosensing. In the next chapter, we will discuss approaches to extend the use of nanoplasmonic interferometry technique for highly-multiplexed detection in imaging mode.

Chapter 4

Plasmonic interferometers for array-based high-throughput sensing

4.1 Scaling up plasmonic sensors for multiplexed sensing in imaging mode

High-throughput biochemical sensing is needed in many important areas such as life sciences, drug discovery, medical diagnostics, food safety, and security [72]. High-throughput sensing allows the same solution to be used to monitor hundreds or thousands of channels at the same time, providing a huge saving in time and also a tremendous cost savings for the precious biomolecules used for these assays. Moreover, because the buffer solution and temperature and many other variables are the same for thousands of sensing spots, this approach offers an improvement in measurement reliability [21]. The use of reference channels also provide effective reduction of noise sources such as non-specific molecular bindings. As we introduced in Chapter 1, while SPR imaging has been successfully commercialized for high-throughput sensing, this technique has several limitations that need to be overcome. The utilization of prism in SPR imaging limits the use of high NA optics and magnification of the imaging system. This has not only limited the throughput of the system but also lowers the sensor signal-to-noise ratio as a smaller number of CCD pixels can be used for a specific sensing spot size. Also the propagation of SPPs from nearby sensing spots is another noise source for SPR imaging. As a result,

the development of SPR imaging systems with both high sensing resolution and small sensing spot size (high throughput capability) is still a challenging task.

Nanoplasmonic sensors are widely believed to be a promising platform to overcome these limitations of SPR imaging due to the simple collinear transmission setup and small nanostructure-based sensor footprint [17-19]. However, so far, most reported work on nanoplasmonic sensors have focused on spectral interrogation method due to its demonstrated superior performance [19,73,74]. While this modulation method is the most straightforward sensing approach to monitor the spectral shifts of plasmon peaks, it requires the sensor array to detect multiple binding events sequentially rather than simultaneously [75,76], making it unsuitable for those applications where high temporal resolution and spatial resolution are required simultaneously [77]. Intensity-based CCD imaging has been suggested as an attractive approach to overcome this limitation by simultaneously providing spatial and temporal information [10,11,77]. Ideally, it is desirable for the nanoplasmonic sensor platform to have both functionalities: a superior spectral sensing capacity comparable to conventional SPR systems, and an intensity-based sensing capacity for scalable multichannel sensing applications. However, the development of such a platform poses significant challenges because of the broad resonance linewidths of existing LSPR and nanohole array sensors, which are associated with the strong radiative damping and absorption losses in the metal [33,49]. These significantly degrade the performance of nanoplasmonic sensors for both spectral sensing and intensity-based imaging.

In Chapter 3, we have demonstrated the superior sensing performance of our prototype plasmonic MZI sensor device. In this chapter, we will further extend the use of plasmonic interferometers to multiplexed high-throughput assay. As the demonstrate plamsonic MZI utilizes a non-collinear transmission setup, we have modified the plamsonic interferometer design, which contains a groove-slit-groove nanostructure and will be especially suitable for high-throughput sensing due to its collinear transmission setup. In this chapter, spectral modulation will first be employed to provide direct insight into several important sensor properties of the modified plamsonic interferometer, including the peak linewidth and refractive index sensitivity, and to guide a rational design and optimization of the sensor platform. The optimized sensor array platform will then be extended to intensity-modulated multiplexed assays, using a CCD camera to simultaneously monitor the narrow-band transmission intensities through multiple sensor elements. A novel self-reference method will also be introduced to approximately double the sensor sensitivity while effectively decreasing sensor noises.

4.2 Design and fabrication of array-based nanoplasmonic interferometers

The proposed modified plasmonic interferometer, shown schematically in Fig. 4.1, illustrates the compact groove-slit-groove nanostructure design. Our sample consists of a 350 nm silver film deposited onto a previously cleaned microscope cover slide. FIB milling was used to fabricate a series of nanoplasmonic interferometers with varying slit-groove distance L. The 30-μm-long slit is at the center of the two 30-μm-long grooves. The slit and groove widths are 100 and 120 nm, respectively. The groove depth is around 70 nm, measured using atomic force microscopy (AFM) (NT-MDT Solver NEXT). Fig.

4.1b shows a SEM image of a fabricated device with L = 5.1 μm. The structure was illuminated normally through the substrate by a focused white light beam. Under TM-polarized illumination (with the electric field perpendicular to the long axis of the slit), light transmitted through the central nanoslit causes SPPs to be launched on the upper metal surface and propagate toward the two nanogrooves. The SPPs are partially reflected back toward the central slit, where they are then scattered and interfere with the light directly transmitted through the slit (Fig. 4.1c). Here two nanogrooves are employed to double the reflected SPP intensities relative to a single-groove interferometer [43,44] and improve the interference contrast. The SPP-mediated scattered light was then collected by an X40 objective for measurement. Illumination of this interferometer platform from the substrate side allows the incident light to be coupled first into a guided mode inside the nanoslit cavity, which has a large acceptance angle for light coupling [78]. As a result, a focused intense optical beam can be used to increase the signal-to-noise ratio of the transmission spectrum, which is especially useful for a small-footprint sensor with limited light transmission [73]. This is a unique advantage of this design over previous plasmonic interferometers, which typically employ collimated illumination on the front side of the nanostructures [44, 79-81]. Moreover, the nanoslit in this device functions as a broadband SPP coupler, which enables sensor operation over a broad spectral range and permits multispectral sensing schemes that have improved sensitivities [57,82].

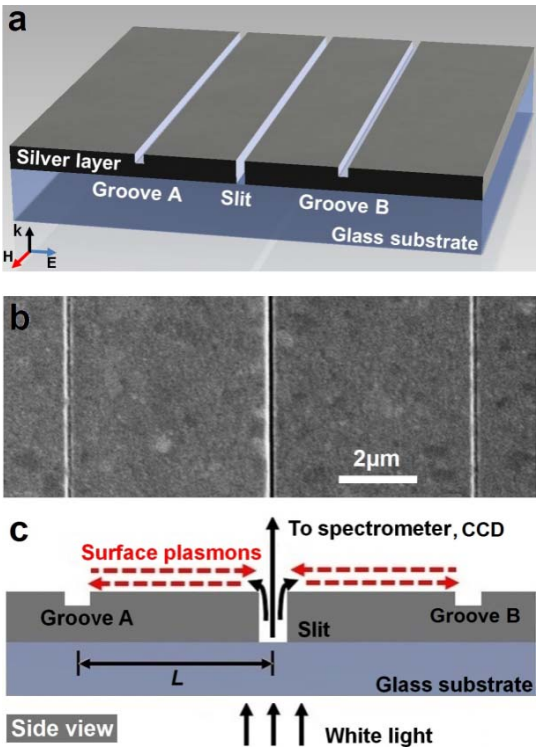

Fig. 4.1. (a) Schematic of the proposed plasmonic interferometer. (b) An SEM image of a fabricated groove-slit-groove nanostructure with L = 5.1 μm. (c) Side view of the proposed interferometer structure.

The solid curves in Fig. 4.2 are experimental spectra measured in an air environment using two interferometers with slit-groove separations of 5.1 and 9.0 μm. Data were normalized to the transmission spectrum of an identical reference nanoslit milled on the same sample. One can see obvious spectral oscillations with narrow peaks and valleys resulting from the constructive and destructive interference between the light transmitted directly through the slit and SPPs propagating between the grooves and the slit. The interference pattern of the interferometer with the larger L of 9.0 μm exhibits faster spectral oscillations with decreased contrast. To better interpret these measurements, similar to Eq. 3.1, theoretical interference patterns can be expressed here as:

$$\frac{I}{I_0} = 1 + \frac{E_{spp}^2}{E_{free}^2} + 2\frac{E_{spp}}{E_{free}}\cos\left(\frac{4\pi L}{\lambda} n_{spp} + \varphi_0\right). \quad (4.1)$$

Here E_{free} and E_{spp} are the field amplitudes of directly transmitted light and SPP modes, respectively. $n_{spp}(\lambda)=\mathrm{Re}((\varepsilon_m n^2/(\varepsilon_m+n^2))^{1/2})$ is the effective refractive index of SPPs at the metal/dielectric interface, ε_m is the metal permittivity, n is the refractive index of the dielectric material on top of the metal surface, and φ_0 is an additional phase shift due to SPP reflection at the grooves and scattering at the slit. According to this equation, the intensity of the transmitted light at a specific wavelength depends on the phase difference between SPPs and free-space light through the term $(4\pi L n_{spp}/\lambda + \varphi_0)$, which can be modulated by bulk refractive index changes or biomolecule adsorptions at the upper sensor surface between the central slit and two grooves. For broadband illumination, a change in refractive index causes a spectral shift of the interference pattern, providing the basis of the proposed sensing scheme. Different from the proposed plamsonic MZI structure in Chapter 3, this modified interferometer design allows the use of collinear transmission setup, suitable for high-throughput multiplexed detection.

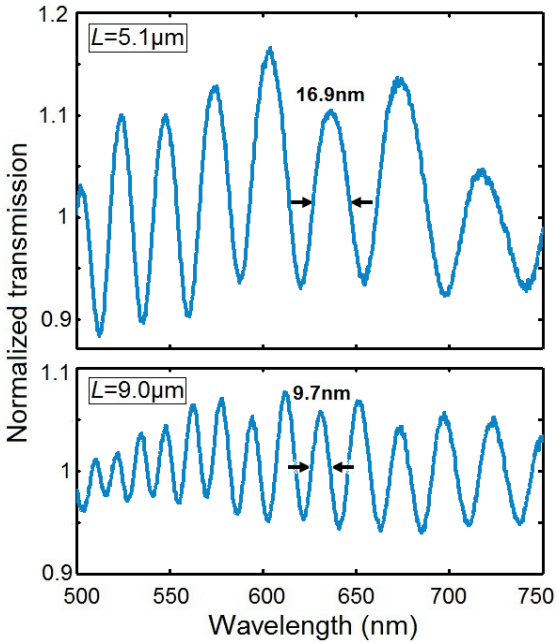

Fig. 4.2. Experimental interference patterns for slit-groove plasmonic interferometers in an air environment with L = 5.1 and 9.0 μm.

By setting the term n_{spp}/λ to constant in Eq. 4.1, we can derive the refractive index sensitivity of this plasmonic sensor as

$$S = \left|\frac{\Delta\lambda}{\Delta n}\right| \approx \lambda\left(\frac{n_{spp}}{n}\right)^3 \Big/ \left(n_{sp} - \lambda\frac{dn_{spp}}{d\lambda}\right). \tag{4.2}$$

Eq. 4.2 predicts that S is approximately 481 nm/RIU in a water environment at a wavelength of 650 nm. A unique advantage of this sensing scheme is the extremely narrow linewidth of the interference oscillation. The peak linewidth, $\delta\lambda$, is defined as half of the oscillation period, P, and can be described by the following equation:

$$\delta\lambda = \frac{P}{2} \approx \lambda^2 \Big/ 4L\left(n_{spp} - \lambda\frac{dn_{spp}}{d\lambda}\right). \tag{4.3}$$

Using Eq. 4.3, one can calculate the peak linewidths to be 16.3 nm (λ ~ 636.1 nm) and 9.1 nm (λ ~ 631.1 nm) for interferometers with L = 5.1 and 9.0 μm in air, respectively,

agreeing well with the experimental results shown in Fig. 4.2. The peak linewidths of plasmonic interferometers are determined by the phase properties of propagating SPPs and free-space light, and can be further narrowed down by increasing L according to Eq. 4.3. This differs from previous nanoplasmonic sensors based on EOT in nanohole arrays or LSPR in nanoparticles, whose resonance linewidths are limited by non-radiative ohmic losses and radiative SPP losses due to scattering. Also note that in this plasmonic interferometer, SPPs travel a round-trip between the slit and groove, which provides half of the peak linewidth observed previously for an interferometer with the same L but using front-side illumination [44,79]. The theoretical FOM of this plasmonic interferometer can be easily derived, yielding

$$FOM = \frac{S}{\delta\lambda} = \frac{4L}{\lambda}\left(\frac{n_{spp}}{n}\right)^3. \tag{4.4}$$

This simple expression predicts that high FOMs are achievable using the proposed sensing scheme. For example, the calculated FOM value reaches 65 for an interferometer with L = 9.0 μm at λ = 650 nm. This would surpass previous EOT-based sensors, which have a typical FOM value of 23 [56].

4.3 Characterization of the sensor performance

To experimentally demonstrate the theoretically predicted sensor performance, we integrated our sample with a PDMS flow cell and injected a series of glycerol-water solutions with different refractive index. As shown in Fig. 4.3a, the interference patterns of interferometers with two different L both red-shift as the liquid refractive index increases. The peak positions were extracted using a Lorentzian fitting method and

plotted in Fig. 4.3b as a function of time. For clarity, the sensor response of the interferometer with L = 5.1 μm was vertically displaced by 2 nm in this plot. As seen in Fig. 4.3b, both interferometers exhibit stable peak wavelengths at each glycerol concentration and the peak shifts were approximately proportional to the increase in glycerol concentration. The sensing peaks return to their initial spectral positions for both interferometers with the final DI water injection. The lower inset of Fig. 4.3b shows the peak positions as a function of the liquid refractive index. The solid lines are the linear fits to the experimental data, providing sensitivities of the two sensors. For interferometers with L = 5.1 and 9.0 μm, the measured sensitivities are 488.7 and 469.1 nm/RIU, respectively, with peak linewidths of 13.9 and 7.0 nm, and FOMs of 35.2 and 67.0, respectively, all in good agreement with the theoretical predictions (see Table 2).

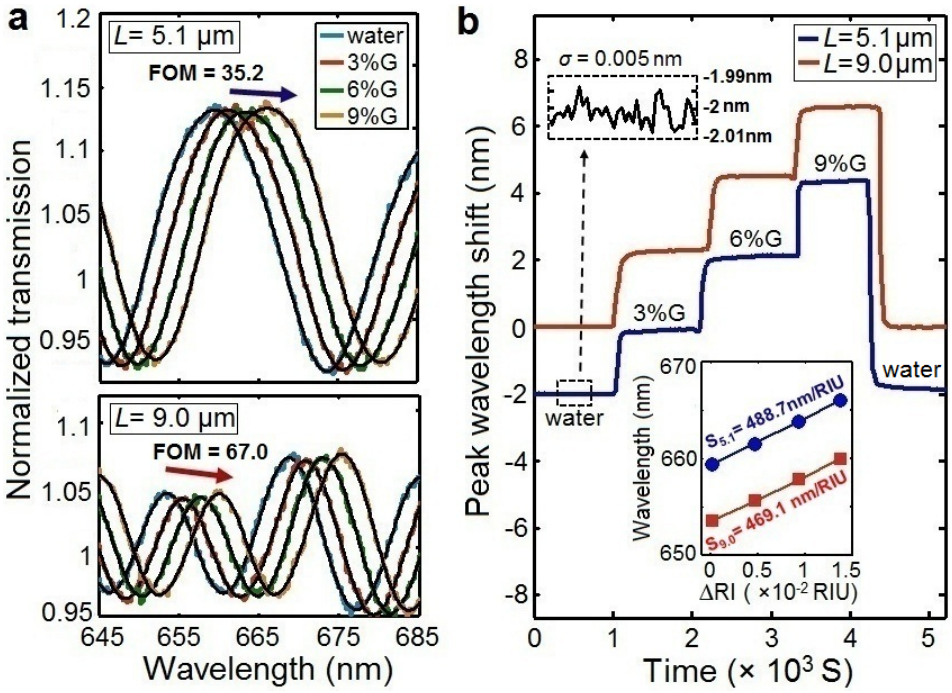

Fig. 4.3. (a) Measured interference patterns of nanoplasmonic interferometers for water and 3, 6, and 9% glycerol-water solutions. Black curves imposed on the raw data are

guides to the eye. The directions of the arrows indicate the red-shifts of the interference patterns. (b) The monitored peak positions for two interferometers as a function of time. The response of the interferometer with L = 5.1 μm was vertically displaced by 2 nm for clarity. The upper inset indicates the sensor noise level and the lower inset shows the spectral positions of the interference peak versus liquid refractive index.

L(μm)	Peak λ (nm)	Sensitivity (nm/RIU)	linewidth (nm)	FOM
5.1	659.4	488.7	13.9	35.2
		484.7	*13.4*	*36.2*
9.0	653.6	469.1	7.0	67.0
		482.2	*7.4*	*65.2*

[a] Numbers in italics are theoretically calculated results.

Table 2. Experimental and Calculated Sensing Performances for Interferometers with Two different values of L.[a]

As shown in the upper inset of Fig. 4.3b, the standard deviation (σ) of the monitored peak wavelength of the interferometer (L = 5.1 μm) is around 5×10^{-3} nm, corresponding to a sensor resolution of 1×10^{-5} RIU [i.e., 5×10^{-3} nm/ (488.7 nm/RIU)]. Importantly, this resolution was measured from a miniaturized sensing area of 30×10 μm^2 using a compact fiber-optic spectrometer. In previous EOT-based nanoplasmonic sensors, similar spectral resolutions have been achieved but typically require collecting higher light levels from sensing areas at least two orders of magnitude larger [57,82], which limits the multiplexing capacity and prevents the integration with compact microfluidics. The good trade-off achieved between the sensor performance and footprint of this plasmonic interferometer was possible because of the narrow interference sensing peaks, and also from the intense focused beam illumination. It should also be noted that, while the interferometer with L of 9.0 μm has a larger FOM of 67, it exhibits very similar sensor resolution as the interferometer with L of 5.1 μm (data not shown). This is due to the

increased SPP propagation loss for larger *L,* which results in a lower spectral modulation depth. From this result one can see that while FOM may be a useful metric in comparing the sensing properties of different nanostructures, it is not the only guide for optimizing sensor performance. The sensor footprint, sensing peak intensity, and spectral modulation depth should also be taken into consideration when optimizing the performance of nanoplasmonic sensors. Due to the smaller footprint, the interferometer with *L* of 5.1 μm will be employed in this work for biosensing and multiplexing experiments in the following sections.

Further optimization of this interferometric sensor is primarily limited by the relatively low interference contrast caused by the unbalanced intensities of interfering SPPs and light. We now discuss reasons for such intensity imbalance and possible ways to optimize it. According to Lalanne's theory [83] and our following experimental validation [44], a large portion of the slit-guided mode (up to ~ 40 %) can be coupled to propagating SPPs (with the rest 60 % scattered into free-space light) when the slit width is around 20 % of the incident wavelength. As a result, we employed an optimized slit width of 100 nm in this work (660 nm × 20% / 1.33 = 99 nm, where the width is scaled by 1.33 as the device is in a water environment). Under this optimized condition, the intensity of the generated SPPs is comparable to interfering free-space light. Therefore, the relatively low modulation depth results mainly from the SPP reflection loss at the nanogrooves and propagation loss at the sensor surface. Here we mention several potentially important improvements that could reduce these losses. First, SPP reflection efficiency at the two grooves can be enhanced by improving the quality of the fabricated grooves (e.g., using

Ag-Al double metal layers with the bottom Al layer as a slow etch rate FIB stop to precisely and uniformly control the fabricated groove depth [84]). Second, instead of using single grooves as reflectors, groove or ridge arrays can be designed to function as Bragg mirrors, which have been shown to provide reflection efficiencies larger than 90% after structural optimization [85,86]. Note that a greater number of grooves or ridges make this interferometer less suitable for broadband sensor operation, but do not affect narrow-band intensity-interrogated sensing as will be discussed in the next section. Third, SPP propagation loss can be reduced by employing ultrasmooth metal films obtained by template stripping [62,82]. Fourth, the sensor noise level could be further reduced by using a more advanced spectrometer with higher saturation level and lower dark noise [73].

4.4 Imaging-based high-throughput sensing experiment

While the capability of this interferometer platform for single-channel sensing has been demonstrated, the spectral modulation method is not suitable for dynamic, highly multiplexed sensing, which requires simultaneous determination of light intensities transmitted through multiple sensing elements. In this section, we further perform real-time, multiplexed sensing experiments using a CCD camera and a narrow band light source for intensity-modulated measurement. As a proof-of-concept demonstration, we fabricated a 4 × 3 array of the slit-groove plasmonic interferometer (Fig. 4.5a). Interferometers in the first and third (second and fourth) column of the microarray have a groove-slit distance, L, of 5.1 (5.2) μm. Fig. 4.5b and c show an SEM image of the fabricated sensor array and a CCD image of one of the plasmonic interferometers,

respectively. Each interferometer has a footprint of around 300 μm^2 with the center-to-center distance between each sensing element of 50 μm, giving a potential packing density of 4 × 10^4 sensors per cm^2. The dense packing capability of the proposed sensing scheme greatly exceeds that of commercial SPR imagers and illustrates its promise for high-throughput microarray applications. Further improvement in this packing density is still possible by fabricating groove/ridge arrays as Bragg mirrors instead of single grooves to enhance SPP reflection efficiency and decrease crosstalk between sensor elements [10].

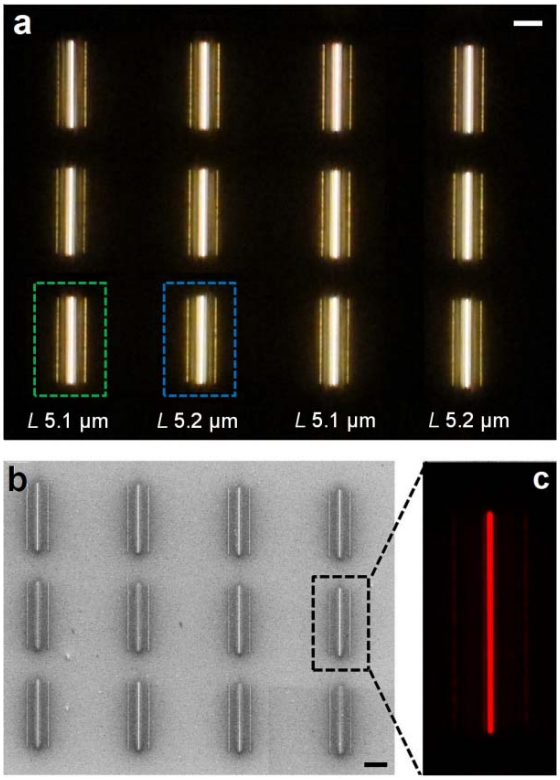

Fig. 4.5. (a) A bright-field microscope image of the fabricated plasmonic interferometer array. Scale bar: 10 μm. The interferometers are fabricated with two different *L*: 5.1 (the first and third column) and 5.2 μm (the second and fourth column) (b) An SEM image of the 4 × 3 microarray. Scale bar: 10 μm. (c) A CCD image of one of the interferometers.

For the imaging experiment, the fabricated sensor array was illuminated through the substrate using a white light source passing through an optical band-pass filter centered at 655 nm with a 12 nm bandwidth. The transmitted light from 12 interferometers was then collected simultaneously by an X40 microscope objective and imaged onto a CCD camera. The intensity change of the transmitted light from each interferometer is determined by two factors: one is the peak shift resulting from refractive index changes and the other is the slope of the spectrum at the illumination wavelength. Accordingly, to achieve optimal sensing performance, the slit-groove distance needs to be carefully designed to locate the high-slope region of the interference pattern at the illumination wavelength. Plasmonic interferometers with L of 5.1 and 5.2 μm are used in this measurement, and their transmission spectra are shown in Fig. 4.6a, respectively. The yellow regions indicate the spectral range of the incident light. Both interference patterns red-shift with the increase in the liquid refractive index, and the transmitted light intensities either increase or decrease, depending on the negative or positive slope of the spectrum. Green and blue dots in the inset of Fig. 4.6b present real-time experimental measurements of the transmitted intensities from these two interferometers. As a series of glycerol-water solutions with increasing refractive index are injected into the channel, the transmission intensity of the interferometer either decrease (for L = 5.1 μm) or increase (for L = 5.2 μm), in agreement with predictions. Following the 6 % glycerol test, DI water was again introduced into the channel, returning the transmitted intensities to their initial levels and validating the reliability of the sensing performance.

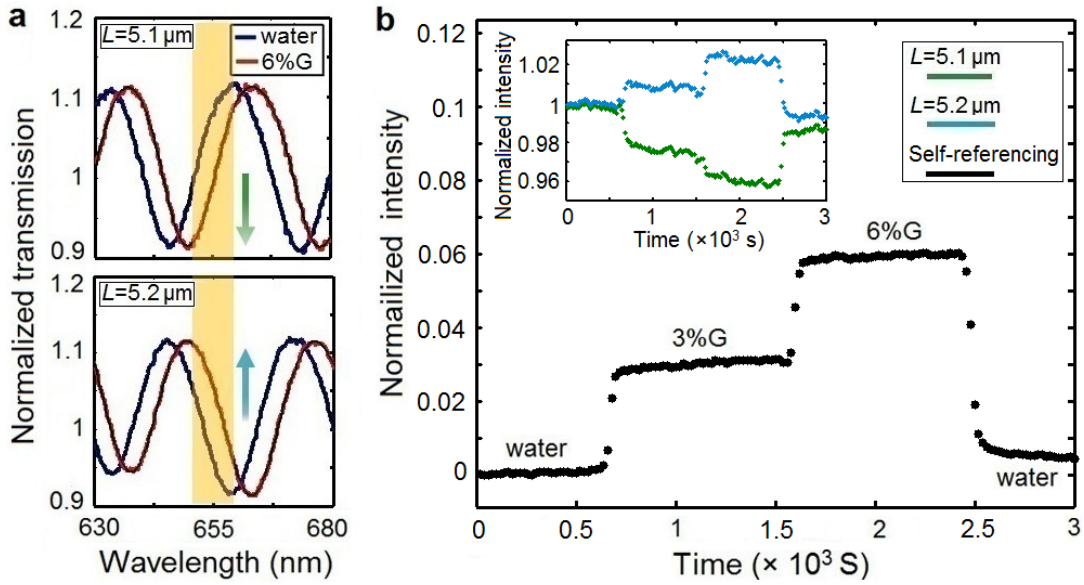

Fig. 4.6. (a) Transmission spectra of interferometers with two different values of L: 5.1 and 5.2 μm. The yellow regions indicate the spectral range of the filtered white light source. As the dielectric refractive index increases, the transmitted intensity can either decrease (L = 5.1 μm) or increase (L = 5.2 μm). (b) The blue and green dots shown in the inset indicate the real-time measurements of the normalized transmitted intensities from two interferometers. The black dots are the experimental results obtained after using a self-referencing method.

The standard deviation of the measured light intensity determines the noise level and detection resolution of this intensity-interrogated sensor. To improve the sensor performance, background fluctuations needs to be subtracted, including noise from mechanical vibrations and light intensity fluctuations. Here a self-referencing method was introduced to reduce the influence of these effects and approximately doubles the sensor sensitivity. As shown in Fig. 4.6a, interferometers carefully designed with two different L exhibit similar initial transmitted intensities but have positive and negative intensity-change sensitivities. To design such two sensors, the interference pattern of the second interferometer needs to be spectrally shifted by half of an interference period from

the first one. The theoretical expression of ΔL (the difference between L of two sensors) can be easily derived from Eq. 4.1 as: $\Delta L = \lambda / 4n_{spp}$, where λ is the sensor working wavelength. According to this equation, two interferometers with L of 5.1 and 5.2 μm were designed and fabricated for measurements. When performing the experiment, a signal arising from the refractive index change shifts the transmitted intensities of these two sensors in two different directions (that is transmission increase or decrease), while unwanted signal from light intensity fluctuations and mechanical vibrations change two transmitted intensities in the same direction. Monitoring the intensity difference between the two interferometers results in a near two-fold improvement in sensor sensitivity, and also subtracts the background noises (see the black dots in Fig. 4.6b). The resulting intensity sensitivity is 684 %/RIU with a sensor noise level of 0.033 %. Here the transmission intensity through single interferometer in water serves as the reference intensity. The sensor resolution is calculated to be 5×10^{-5} RIU (0.033 %/ 684 %/RIU), 6 times smaller than that of a single interferometer (3×10^{-4} RIU for the interferometer with $L = 5.1$ μm).

This demonstrated sensor resolution is better than previous nanohole array-based multiplexed sensors, with typical refractive index resolutions in the 10^{-4} RIU range. Importantly, this demonstrated sensor sensitivity and resolution can be improved by increasing the interference contrast through the methods discussed in section 4.3. Instead of a halogen lamp, an intense and highly stable laser source may also be used to reduce the light source fluctuation and further increase the sensor signal-to-noise ratio. In addition, the dynamic range is also an important sensor characteristic. The dynamic range

of this sensor is around 0.01 RIU (the refractive index difference between water and 6 % water-glycerol mixture) using the current experimental setup. The dynamic range of this interferometric sensor depends on the bandwidth of the incident light and also the interference linewidth. By setting up a laser to replace the current 12-nm-bandwidth light source, the dynamic range of the device can be improved. Also, by increasing the interference linewidth through tuning L (see Eq. 4.3), the dynamic range of the device can be further increased. Note that the increased linewidth might lead to lower intensity sensitivity. Thus, one needs to rationally design L to balance such trade-off between the sensor performance and dynamic range with regard to the target applications. Large-area fabrication of the proposed sensor device is also important for future practical applications. While the FIB fabrication method used in this work is not applicable to large-area patterning, emerging nanofabrication techniques such as template stripping [87] allows mass production of the proposed three-dimensional silt-groove nanostructures.

4.5 Summary

In summary, we have demonstrated real-time, multiplexed sensing in this chapter using nanoplasmonic interferometric sensors. The SPP-light interference results in narrow sensing peak linewidths of 7 nm and provides a new route for plasmon line shape engineering by tailoring interferometer structures as well as SPP amplitude and phase properties in two interfering channels. A refractive index resolution of 1×10^{-5} RIU has been measured from a miniaturized sensing area of 30×10 μm^2 using a low-cost spectrometer. This sensor resolution can be further improved by fabricating large-area

interferometer arrays, employing an advanced spectrometer, or using multiple groove/ridges to increase SPP reflection efficiencies at the groove reflectors. We have demonstrated the high-throughput, multiplexed sensing capability of this small-footprint sensor by using a CCD camera and a narrow band light source for intensity interrogation. The demonstrated multiplexed sensing performance and possible further improvements suggest that this novel class of nanoplasmonic interferometric sensors have exciting promise to be integrated into multiplexed, miniaturized sensing devices for label-free biochemical applications.

Chapter 5

Optimization of plasmonic interferometers for sensing and high-throughput imaging

In Chapter 3 and 4, we have demonstrated the single-channel sensing and multiplexed imaging capacity of the proposed plamsonic interferometer platform. While demonstrated sensor characteristics (refractive index sensitivity, FOM) greatly exceed that of existing nanoplasmonic sensors, the overall sensor performance (sensor resolution) is still not comparable to commercial prism-coupling SPR systems. For example, the plasmonic MZI exhibits a sensor resolution of 7.5×10^{-6} RIU, one to two orders larger than that of state-of-the-art SPR system (1×10^{-7} RIU). The demonstrated slit-groove plasmonic interferometer array shows a sensor resolution of 5×10^{-5} RIU for imaging-based multiplexed detection, 5 times poorer than that of commercial SPR imagers. In this chapter, we further optimize the plasmonic interferometer design to achieve bold advances in both single-channel spectral sensing and imaging-based multiplexed detection. The demonstrate optimized sensor platform exhibits a spectral sensing performance comparable to state-of-the-art commercial SPR systems, as well as a record high intensity-change sensitivity that is promising for scalable high-throughput sensing applications. The proposed optimized sensor device has a simple structure design, which consists of concentric nanogrooves that function as a plasmonic lens [88] and a central

aperture patterned on a gold film. When the whole structure is illuminated by a collimated white light beam, the plasmonic lens excites and focuses SPPs to the central aperture, where the SPPs interfere with the light that is directly transmitted through the aperture and modulate the far-field transmission. By careful structural tuning, we can effectively control the phase and intensity properties of interfering SPPs and light to generate spectral fringes with high contrast, narrow linewidth, and large amplitude, all key characteristics to achieve optimized spectral sensing. Using this method, we have demonstrated a superior protein surface coverage resolution of 0.4 pg/mm^2. This resolution compares favorably with that of commercial SPR systems (0.1 pg/mm^2) [4], but was achieved here using a significantly simpler optical transmission geometry, a two orders of magnitude smaller sensor footprint, and a low-cost compact fiber-optic spectrometer. Moreover, we further introduced in this chapter a low-background intensity-based sensing concept, which can be easily combined with CCD imaging to scale up our sensor platform to high-throughput assays. It measures the changes in relative intensity (dI/I_0) induced by a refractive index change dn at a specific wavelength. A widely employed figure of merit, defined as FOM* = $(dI/I_0)/dn$, is used to evaluate the intensity-based sensor performance [89-91]. Our approach exploits the near-dark reference background ($I_0 \sim 0$) achieved through balanced destructive SPP-light interference, and yields a record high FOM* value of 146 in the visible region. The demonstrated platform using this novel sensing method show a sensor resolution of 1×10^{-5} RIU, comparable to commercial SPR imagers but based on a two orders of magnitude smaller sensor footprint. In the following, we will first introduce the detection

principle of this optimized circular plasmonic interferometer and then show the demonstrated superior performance for both single-channel and multiplexed sensing.

5.1 A circular nanoplasmonic interferometer with optimized performance for both sensing and imaging

5.1.1 Design of circular nanoplamsonic interferometer

The proposed optimized interferometer structure, schematically illustrated in Fig. 5.1a and b, consists of a gold film containing a nanoaperture surrounded by three nanopatterned concentric grooves. While silver exhibits lower SPP propagation loss and was employed in previous nanoplasmonic interferometers [34,35,44,79], here we employ gold for its superior stability and biocompatablity for biosensing applications. The multiple circular grooves function as an efficient SPP coupler as well as a focusing lens to scatter the normally incident light into propagating SPPs and then focus them at the central hole [92]. The groove periodicity (P) is carefully chosen so that the SPPs launched at each groove add up approximately in phase in the spectral region of interest, generating a strong propagating SPP wave directed to the central focusing point. The following simple expression may be used to calculate P [93]:

$$P = \lambda \sqrt{\frac{\varepsilon_m + n^2}{\varepsilon_m n^2}}, \tag{5.1}$$

where λ is the center wavelength of the spectral region of interest, ε_m is the gold permittivity, and n is the refractive index of the medium covering the sensor surface. At the hole position, the focused SPPs interfere with the light that is directly transmitted

through the hole and modulate the far-field scattering. The theoretical expression for the transmitted light intensity through the interferometer can be written as:

$$I = E_{light}^2 + E_{spp}^2 + 2E_{light}E_{spp}\cos\left(\frac{2\pi R}{\lambda}n_{spp} + \varphi_0\right). \quad (5.2)$$

Here E_{spp} and E_{light} are the field amplitudes of SPP-mediated and directly-transmitted light components at the central aperture, respectively. R is the distance between the middle circular groove and the rim of the hole. n_{spp} = Re $((\varepsilon_m n^2/ (\varepsilon_m+n^2))^{1/2})$ is the effective refractive index of SPPs propagating along the metal surface between the grooves and the hole, and φ_0 is an additional phase shift associated with SPP excitation at the grooves. The term $(2\pi R n_{spp}/\lambda + \varphi_0)$ represents the phase difference between the two interfering components, which varies with λ and leads to constructive and destructive SPP-light interferences. The spectral positions of the resulting multiple interference peaks and valleys are very sensitive to n_{spp}, which can be modulated by surface biomolecular adsorption.

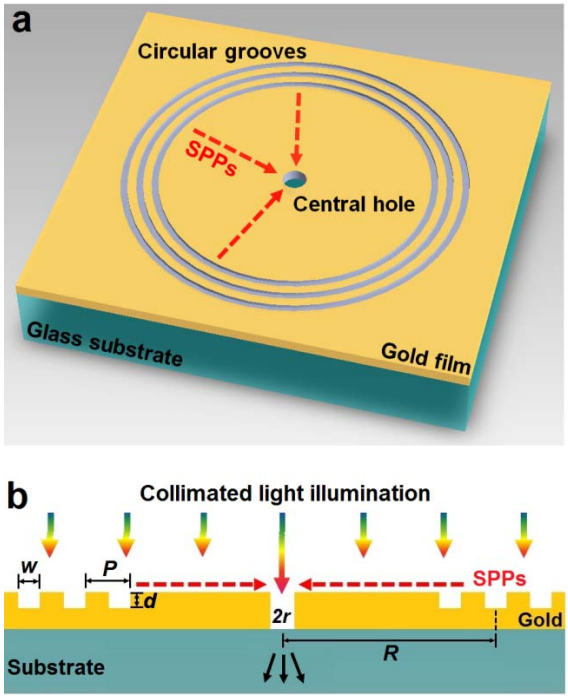

Fig. 5.1 The working principle of the plasmonic interferometer. (a) Schematic of the proposed plasmonic interferometer. (b) Side view and the operating principle of the device.

In the context of sensor design, there are several important structural parameters that largely determine the device performance. Using Eq. 5.2, we can derive the expression for the interference linewidth $\delta\lambda$, defined here as half of the spectral oscillation period:

$$\delta\lambda \approx \lambda^2 \Big/ 2R\left(n_{spp} - \lambda\frac{dn_{spp}}{d\lambda}\right). \tag{5.3}$$

As suggested by this equation and experimentally demonstrated in Ref 35, the interference peaks and valleys can easily be made narrower by increasing the SPP path length R. Note that adjusting R also allows the focused SPP intensity to be tuned through SPP propagation loss. Since the hole radius (r) can also be varied to control the intensity

of the directly transmitted light, the geometric parameters can thus be strategically designed to approximately balance the intensities of two interfering components in the spectral range of interest. The resulting spectral fringes with high contrast and relatively narrow linewidths are especially favorable for enhanced spectral sensing. Another important design parameter is the number of the groove couplers. Previous studies on plasmonic interferometry have investigated using a single linear nanoslit or nanogroove to excite SPPs [34,35,44,79,94]. While this approach allows SPP coupling over a broad wavelength range, the generated SPP energy is likely insufficient for further optimization of the device performance. Our structural design goes beyond previous plasmonic interferometers by introducing multiple circular groove couplers to generate significantly stronger focused SPPs. This offers more degrees of freedom to optimize and balance the intensities of two interfering components and generates high-contrast interference fringes. Also, this unique design differs from traditional bull's eye structures that use a periodic Bragg grating for resonant scattering and focus on transmission enhancement only for a single wavelength or a narrow wavelength range [92,93]. As will be discussed in the next section, here we choose three nanogrooves to balance the trade-off between SPP intensity and sensor working spectral range. The fast spectral oscillation produced over a relatively broad wavelength range serves as a unique advantage of this sensor for optimized spectral sensing.

5.1.2 FDTD numerical modeling

To examine the interplay between multiple geometric parameters and the device characteristics, we performed three-dimensional finite difference time domain (FDTD)

numerical simulations (Lumerical Solutions Inc.). The dielectric constant of gold used in the simulations was experimentally measured using an ellipsometer (J. A. Woollam, V-VASE) and shown in Fig. 5.2. The perfectly matched layer boundary condition was used in x, y and z axes in our 3D simulations. A mesh size of 2 nm was utilized. For the parameter optimization process, the preferred groove depth d and width w can be first determined using simulations to maximize the SPP coupling efficiency. Since the white light source used has its maximum power around λ = 625 nm, the value of P corresponding to this wavelength was calculated using Eq. 5.1 and found to be 430 nm. The parameters R and r were then carefully tuned with the goal of using the largest possible R, while still balancing the intensities of two interfering components. These simulations yielded an optimal geometric parameter set (R = 4.3 μm, w = 200 nm, d = 45 nm, P = 430 nm, and r = 310 nm) with interfering components perfectly balanced in power and generating broadband, high-contrast, narrow-linewidth spectral interference (see the simulation result in Fig. 5.3a). Fig. 5.3b and c show the calculated electric field distributions at the interference peak and valley wavelengths, respectively. Fig. 5.4 also shows the distribution of $|E_x|$ and $|E_z|$ components, respectively. Strong light transmission and perfect light cancellation are clearly visualized at the central hole location, which correspond to constructive and destructive SPP-light interferences, respectively.

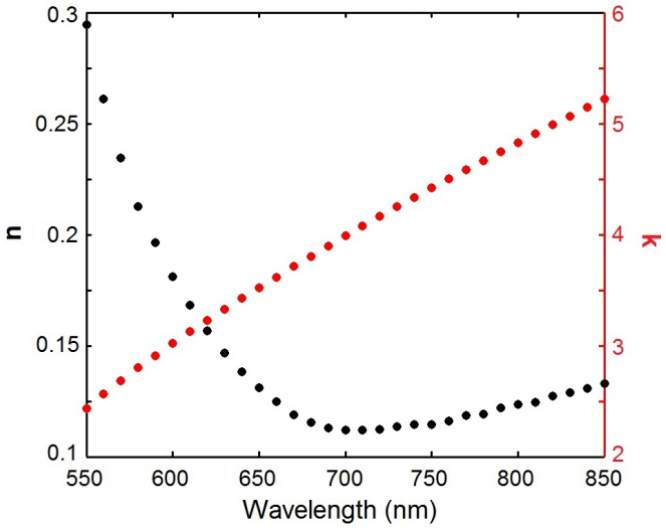

Fig. 5.2. Measured *n* and *k* of the gold film used in the experiments. Measured by J. A. Woollam, V-VASE ellipsometer.

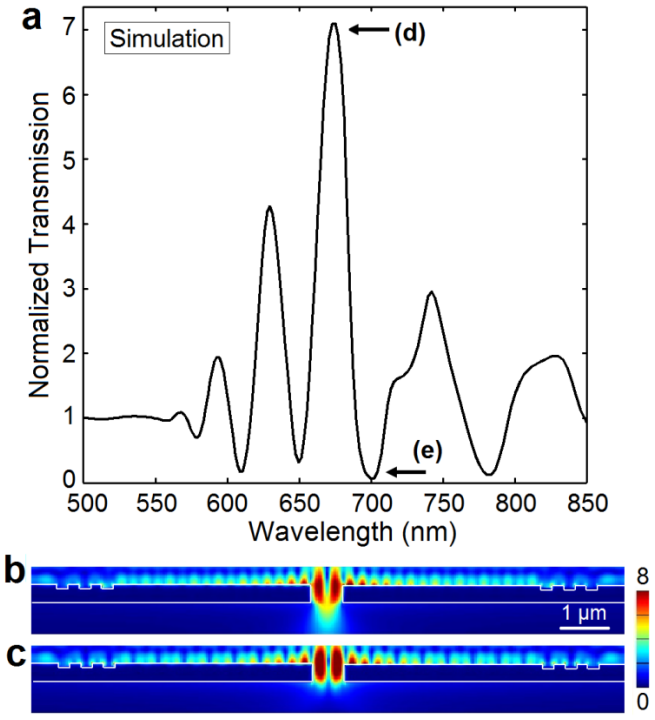

Fig. 5.3. (a) The simulated transmission spectrum of the proposed interferometer, normalized to that of a reference central aperture. The calculated electric field

distributions (|E|/|E_0|) at interference peak and valley wavelengths are plotted in (b) and (c), respectively.

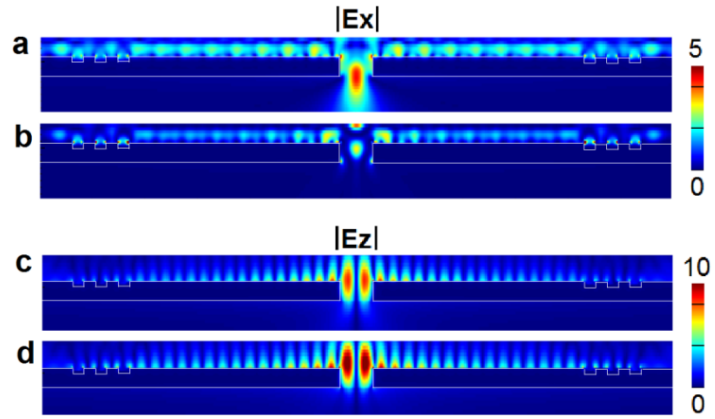

Fig. 5.4. Calculated $|E_x|$ distributions at interference peak (a) and valley (b) wavelengths. Calculated $|E_z|$ distributions at interference peak (c) and valley (d) wavelengths.

5.1.3 Sensor fabrication and characterization

Following design and optimization of the device geometry, FIB milling was used to mill the plasmonic interferometers. The structures were patterned on a 300 nm-thick gold film deposited on a glass substrate that had been previously coated with a 5 nm titanium adhesion layer. Fig. 5.5a-c show both the SEM images and bright-field microscope image of the fabricated interferometers. Here a large 12 × 12 array of the proposed interferometers was fabricated to improve the overall light transmission and the spectral signal-to-noise ratio. The device was illuminated from above by a collimated white light beam normally incident on the top sample surface. The blue solid curve in Fig. 5.6 shows the measured transmission spectrum of the interferometers in a water environment, normalized to that of a reference hole array without surrounding grooves. This experimental spectrum agrees reasonably well with the simulated result in Fig. 5.3a,

demonstrating the operating principle of the device. The slight discrepancy likely arises from fabrication imperfections due to difficulties in precise control of groove profile, and also from the SPP propagation loss resulting from the gold surface roughness (RMS 2.9 nm measured using AFM, see Fig. 5.7), which is not fully accounted for in the numerical simulations. As one of our major goals is to achieve high modulation contrast for optimized spectral sensing, we now quantify the interference contrast C using the equation $C = (I_{max} - I_{min})/ (I_{max} + I_{min})$ [95]. Here I_{max} and I_{min} are adjacent intensity maximum and minimum of the interference fringe, respectively. Because of the balanced intensities of SPPs and free-space light, the experimental contrast of our interferometers (as high as 0.87) greatly exceeds that observed in previous plasmonic interferometers [34,35,44,79]. However, this is still slightly lower than the simulated interference fringe contrast of 0.98, which result from balanced interfering components as well as a perfectly collimated light illumination. In our experiments, the microscope field and aperture diaphragms were both closed to achieve a near-collimated light illumination condition, which, however, still has 3° light divergence. Higher experimental contrast would be expected by further optimizing the collimating optics.

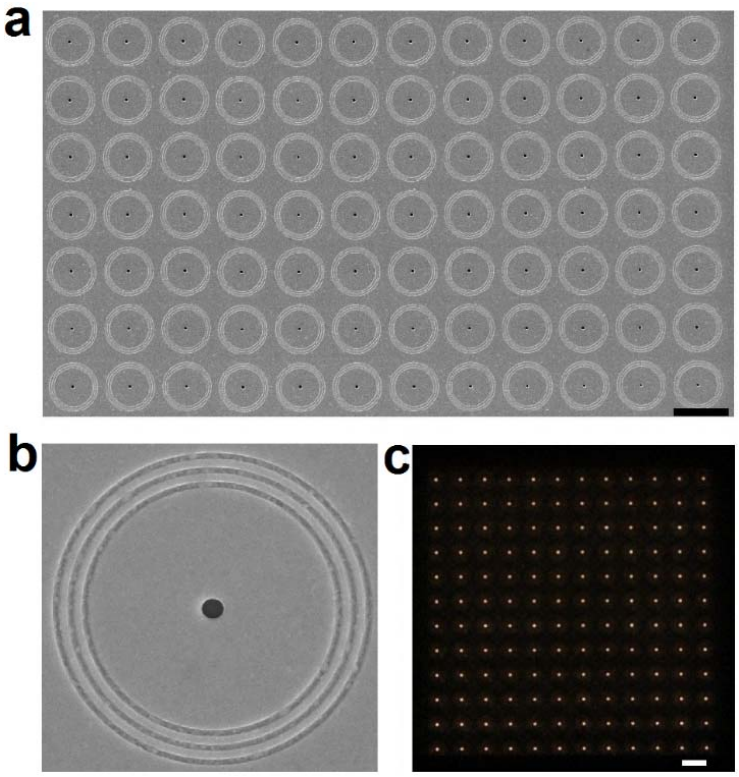

Fig. 5.5. The fabricated interferometer array and the spectroscopy characterization. SEM images of the fabricated interferometer array (a) and one of the interferometers (b). Scale bar: 10 μm. (c) The bright-field microscopy image of the device. The center-to-center distance between each interferometer is 12.5 μm, and the sensor array footprint is 150 × 150 μm^2. Scale bar: 10 μm.

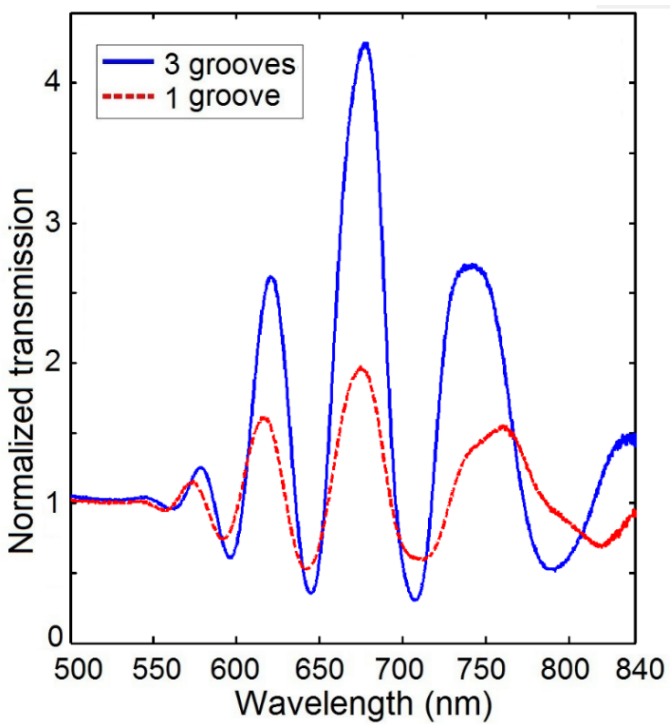

Fig. 5.6 Experimental spectra for plasmonic interferometer arrays with three circular grooves (blue solid curve) and single circular grooves (red dashed curve).

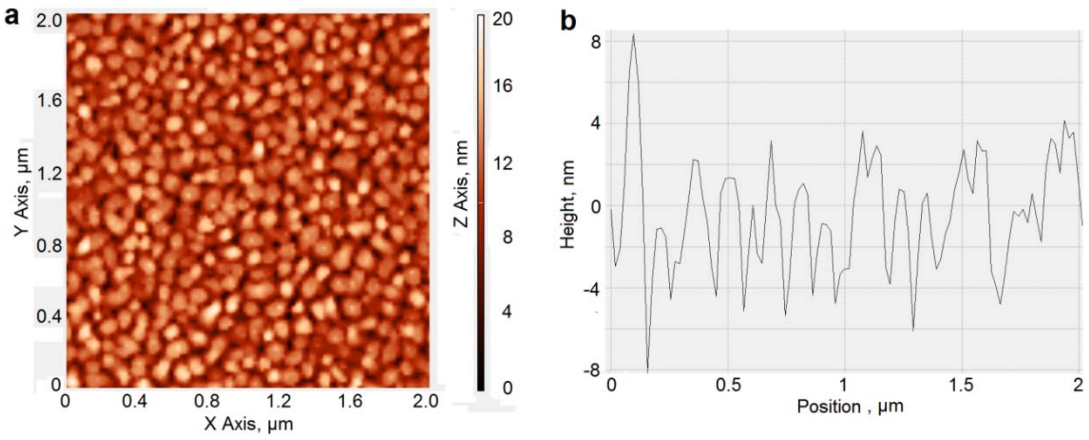

Fig. 5.7. AFM images of a 300 nm gold film. The root mean square roughness is 2.9 nm, measured from a 2 × 2 μm^2 area using a NT-MDT Solver NEXT AFM.

The red dashed curve in Fig. 5.6 shows the measured normalized spectrum of an interferometer array with a single circular groove, which clearly exhibits lower interference contrast. From this result one can see that the use of multiple nanogrooves with properly designed period P increases the generated SPP power and improves the interference amplitude and contrast. Note that while more nanogrooves can be added to further increase the interference peak intensity, the interference contrast decreases when the number of grooves is too high due to resonant Bragg scattering which only efficiently generates SPPs for a specific wavelength. Fig. 5.8a shows the transmission spectra and contrast for a series of interferometers as the number of circular grooves varies from one to six. For interferometers with groove number of 1, 2, 3, 4, 5, and 6, the interference contrasts are 0.56, 0.81, 0.87, 0.84, 0.78, and 0.75, respectively. We now further discuss the origin of such contrast dependence on groove numbers. Since each groove in a circular groove array can excite SPPs but has a different distance to the central aperture, the SPP phase delay from each groove to the aperture is different and leads to slightly different interference patterns. We treat the interference pattern of the hole-grating structure approximately as a superposition of the contributions from each circular groove. Fig. 5.8b shows the interference fringes (calculated using Eq. 5.1) resulting from each groove (green curves) and their superposition (the red curve). It is clear that as the groove number increases from 3 to 5, and to 7, the transmission increases at the valley position (indicated by the black arrows), and accordingly, the interference contrast decreases. In our experimental measurements, the interferometers with three circular grooves exhibit the highest contrast of 0.87. Higher interference contrast is favorable for our multispectral

sensing measurements and especially for low-background intensity-based sensing scheme, as will be discussed later. A smaller groove number has the advantage of overall device compactness and ease of fabrication. As a result, in this work interferometers with three circular grooves were employed for sensing measurements.

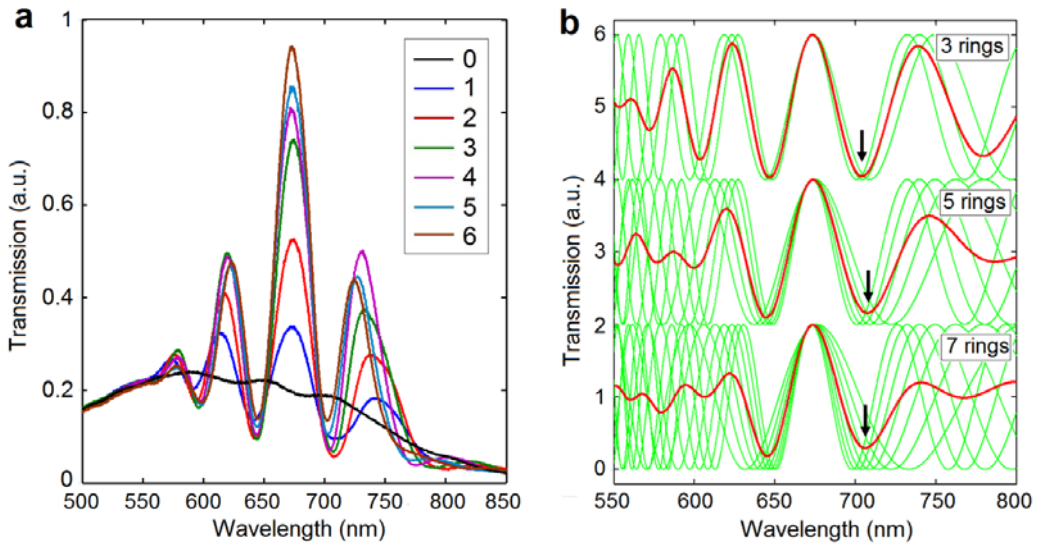

Fig. 5.8. (a) Transmission spectra for interferometers with increasing number of circular grooves from 0 to 6. (b) Analytically calculated interference patterns contributed by each groove (the green curves) and their superposed interference fringe (the red curve).

5.2 High-performance single-channel spectral sensing

Refractive index sensing. To calibrate the sensor sensitivity and resolution, we integrated the fabricated sensor chip with a PDMS microfluidic channel and injected a series of glycerol-water solutions of different refractive index. As shown in Fig. 5.9a, the interference pattern red-shifts upon the increase in liquid refractive index. The signal changes that occur over a broad spectral range constitute a unique advantage of this interferometric sensor. To exploit this sensor property, we use a multispectral data

analysis method, which integrates the magnitude of the relative intensity changes at all wavelengths as the sensor output [57,82]. This approach improves the detection signal-to-noise ratio and sensor resolution, since more SPP-mediated data are taken into account than for the common single-peak tracking method. The integrated response (IR) of the sensor can be expressed as:

$$IR = \sum_{\lambda_1}^{\lambda_2} \left(\left| I(\lambda) - I_0(\lambda) \right| / I_0(\lambda) \right), \tag{5.4}$$

where λ_1 and λ_2 define the wavelength range of the integration, and I_0 is the reference transmitted intensity of the sensor in water. Fig. 5.9b shows the relative intensity changes for liquids of different refractive index. The signals are most prominent in the spectral range from 570 nm to 800 nm, as indicated by the black dashed lines. The magnitude of the intensity changes were integrated within this spectral range, providing the sensor output IR. As shown in Fig. 5.9c, the change in IR is approximately proportional to the increase in glycerol concentration, confirming the excellent sensor linearity. Fig. 5.9d shows the extracted IR values as a function of the refractive index. The linear fit to the data points yields a sensor sensitivity of 2.71×10^6 %/RIU. The lower inset of Fig. 5.9c indicates the noise level of the integrated response, which exhibits a standard deviation of 2.16 % on a time scale of 3 minutes. This corresponds therefore to a bulk refractive index resolution of 8.0×10^{-7} RIU (i.e., 2.16 %/ 2.71×10^6 %/RIU). Note that in this real-time measurement, the time resolution is 10 s (200 spectra are averaged with an integration time of 50 ms for each spectrum). An easy and efficient way to further enhance the detection resolution of a plasmonic sensor using spectral modulation is to increase the

number of spectra averaged, but at the cost of time resolution. For real-time kinetics measurement, care must be taken to balance such trade-off between time and detection resolution. For faster kinetics measurement, a smaller number of spectra can be averaged with a modest increase in the sensor noise level (see Fig. 5.10).

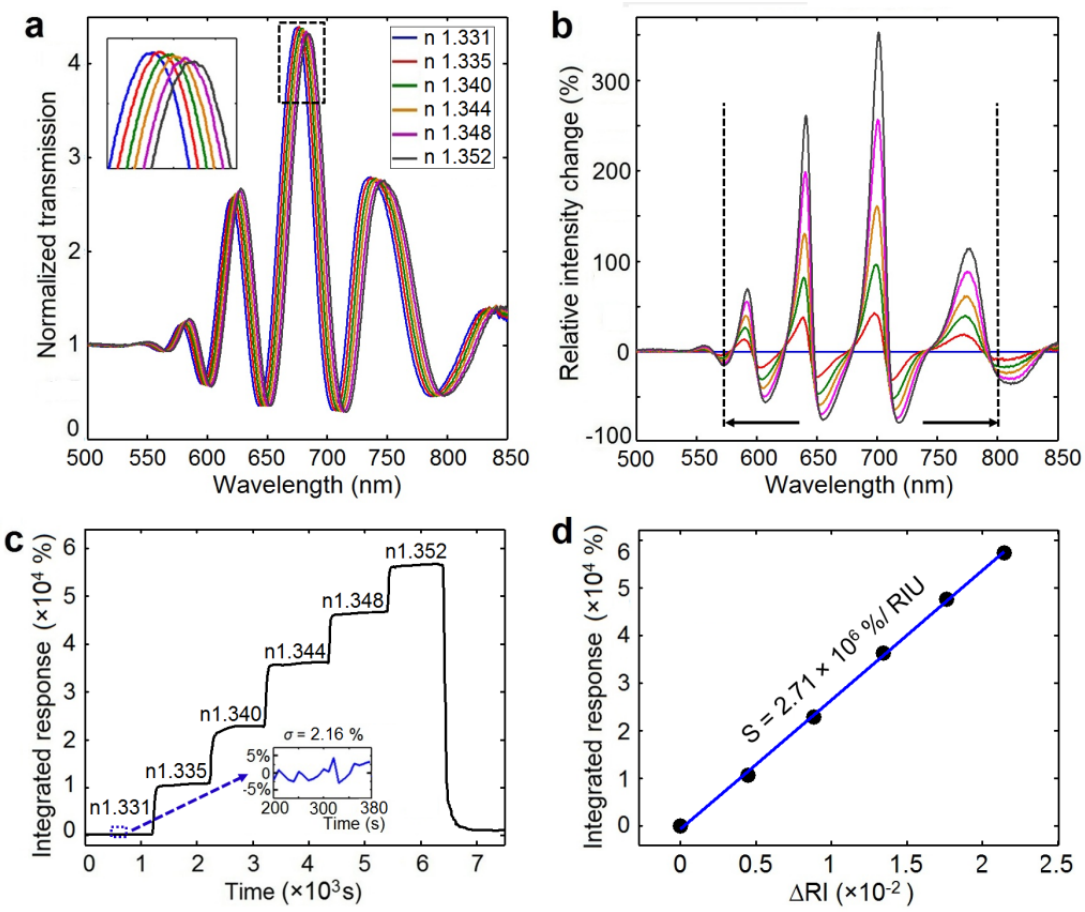

Fig. 5.9. Refractive index sensing using plasmonic interferometer array. (a) The normalized transmission spectra of the interferometer array in water and 3, 6, 9, 12, 15 % glycerol-water mixtures. (b) The relative intensity changes $(I(\lambda) - I_0(\lambda))/ I_0(\lambda)$ for liquids with different refractive index. The dashed lines indicate the spectral region for integration. (c) The integrated sensor response as a function of time. The inset indicates the noise level of the sensor response on a time scale of 3 minutes. (d) The extracted integrated sensor response for liquids with different refractive indices. The blue line is the linear fit to the data points, which shows good sensor linearity.

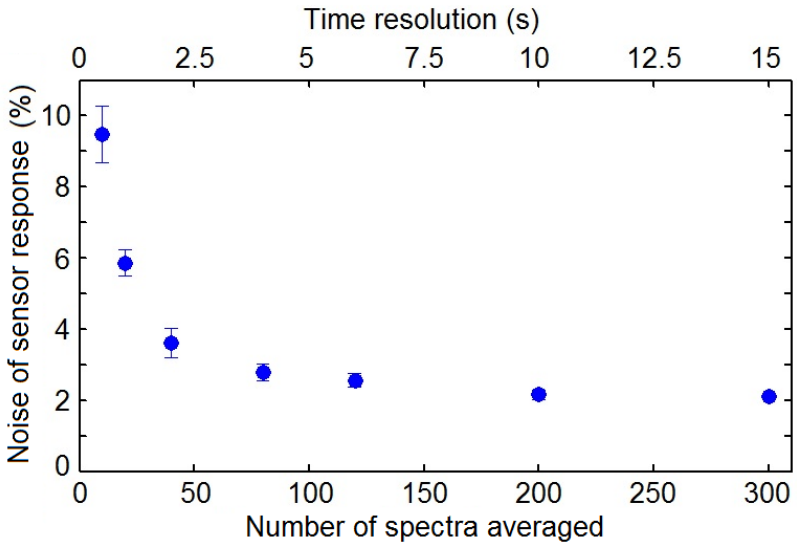

Fig. 5.10. The sensor noise for different number of spectra averaged.

We also measured the sensor resolution by using the common single-peak tracking method. The sensitivity of the interference peak at 674.5 nm is determined to be 470.6 nm/RIU (see Fig. 5.11), and the standard deviation of the peak position is 7.3×10^{-4} nm, corresponding to a sensor resolution of 1.55×10^{-6} RIU. One can see that this multispectral sensing method improves the sensor resolution by approximately two fold. Our demonstrated sensor resolution surpasses that of state-of-the-art nanohole array sensors (3.1×10^{-6} RIU) [96], and is obtained here using a low-cost spectrometer and a simple transmission setup. The improved sensor performance results from the high-contrast, narrow-linewidth interference fringes, the intense transmission peaks from a large interferometer array, and also the broadband sensor response and associated advanced data analysis method. Moreover, several potentially important improvements could further enhance this sensing resolution. First, a larger number of interferometers can be fabricated on a sensor chip using large-area fabrication techniques (i.e., template

stripping on a patterned silicon template [87]) to further increase the spectral signal-to-noise ratio. Second, the interference amplitude is mainly limited by the SPP propagation loss, which could be effectively reduced by employing ultrasmooth metal films [62,82]. Third, a temperature controller can be integrated with the sensor chip to decrease the sensor noise caused by temperature fluctuations.

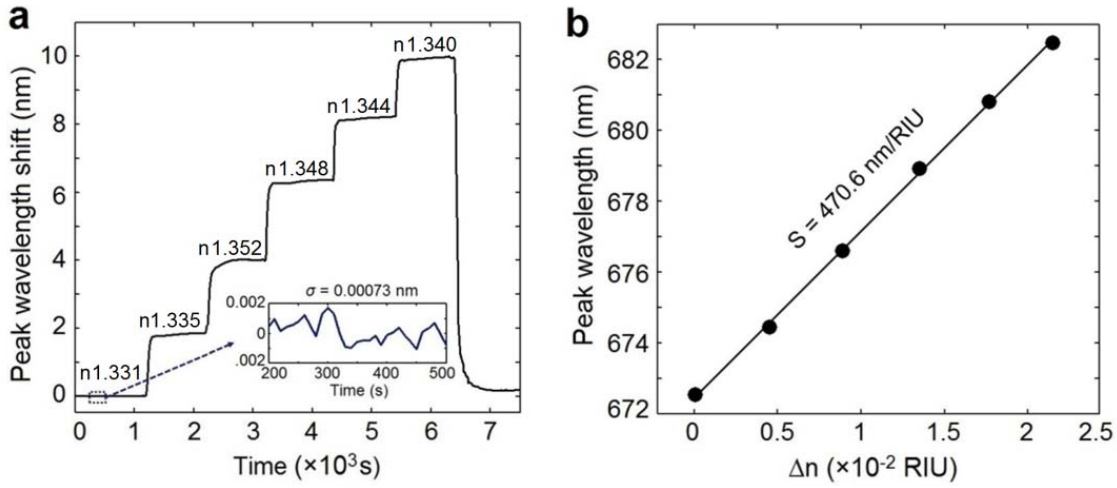

Fig. 5.11. (a) The monitored interference peak position as a function of time. The lower inset shows the standard deviation of the sensor response. (b) The extracted peak position as a function of liquid refractive index.

Real-time biomolecular sensing. While superior bulk sensing resolution was achieved, it does not directly represent the sensor capability for surface biomolecular sensing. In this section, we further demonstrate the feasibility of this platform for biosensing and estimate the biosensing resolution of this optimized sensor platform. We performed label-free real-time monitoring of the specific binding between BSA and anti-BSA molecules. The microfluidic channel was first injected with a PBS buffer for 25 min to rinse the sensor chip and define the experiment baseline. A 500 μg/ml BSA solution in PBS buffer

was then introduced in the channel and functionalized the surface with a monolayer of BSA molecules. As shown in Fig. 5.12, a large sensor integrated response *IR* of 0.91 × 10^4 % was clearly observed (see the first signal change at the time of 1.5 × 10^3 S). A subsequent 15 min buffer wash has little effect on the sensor response. Then, a 42 μg/ml anti-BSA solution was injected in the channel and followed by a 25 min buffer rinse to wash out the unbound anti-BSA molecules. The small spikes observed at buffer injections are measurement artifacts caused by exchanging syringes. The binding between BSA and anti-BSA leads to an *IR* change of 0.62 × 10^4 %. Note that the saturated BSA monolayer, which has a surface coverage of around 1.7 ng/mm^2 [69], was detected here with a high signal-to-noise ratio (SNR) of 4213 (i.e., 0.91 × 10^4 %/ 2.16 %). This high SNR, achieved with a low-cost portable spectrometer, exceeds that of state-of-the-art LSPR biosensors, which exhibit an SNR of ~ 3000 for monolayer protein adsorption and relies on an expensive advanced spectrometer [73]. The SNR of 4213 gives a final sensor resolution of 0.4 pg/mm^2 (i.e., 1.7 ng/mm^2/ 4213) for protein surface coverage. This demonstrated sensor resolution is in fact comparable to that achieved in commercial prism-based SPR systems, which can detect biomolecules down to 0.1 pg/mm^2 from a sensing area of a few mm^2 [4]. It is important to note that our sensor footprint (150 μm × 150 μm) is around two orders of magnitude smaller than that of commercial systems. This largely improved sensor resolution per unit area facilitates sensor integration with compact microfluidics and also decreases the sample consumption. Furthermore, the collinear transmission setup of our platform is much simpler than the total internal reflection operational mode of conventional SPR systems,

and has great potential for system miniaturization, low-cost production, and for scaling up to highly-multiplexed sensing measurements. Finally, further improvement in resolution is still possible by employing the optimization methods discussed in the last section. With demonstrated superior performance and possible further improvement, this simple sensor platform may serve as a promising alternative to conventional bulky expensive SPR devices. Note that in both bulk and bio-sensing experiments, the sensor noise was determined in blank samples (water for bulk sensing and PBS buffer for biosensing). However, for biomolecular detection in complex fluids (serum, urine, etc), other noise terms are present (such as nonspecific biomolecular bindings), and the sensor resolution will depend not only on nanostructure design and optical instrumentation, but also on sensor surface chemistry and sample complexity.

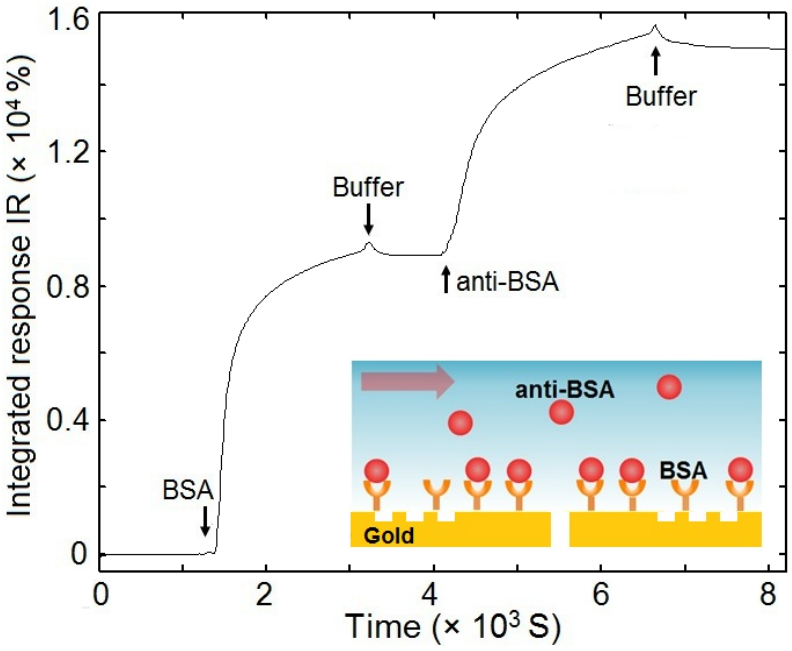

Fig. 5.12. Real-time integrated sensor response upon BSA adsorption on the sensor surface and subsequent molecular binding between BSA and anti-BSA.

5.3 High-performance imaging-based high-throughput sensing

In previous sections, we have demonstrated enhanced sensor performance using a spectral sensing method. However, for applications that require simple and inexpensive instrumentation, biosensing device based on intensity interrogation is typically preferred. More importantly, the intensity-based sensing scheme can be easily combined with CCD imaging to advance our sensor platform for scalable high-throughput sensing applications. In this section, we further investigate the performance of this interferometric platform using intensity interrogation. To better evaluate and compare the sensor performance using this detection scheme, Becker et al. have suggested a figure of merit, defined as [91]:

$$FOM^* = \left| dI / I_0 \right| / dn. \tag{5.5}$$

Here dI/I_0 is the change in relative intensity at an incident wavelength λ induced by a refractive index change dn. For optimized sensing performance, the sensor operating wavelength λ should be properly chosen to maximize the value of FOM*. Our interferometric sensor have a fundamental advantage in that balanced destructive interference between SPPs and free-space light leads to extremely low optical transmission through the interferometers ($I_0 \sim 0$). This delicate interference balance can be easily disrupted by a small change in local refractive index and thus gives rise to a pronounced relative intensity increase dI/I_0 and a corresponding high FOM* value. The near-dark reference background I_0 allows the use of stable high-power laser sources without saturating the detector and produces significantly large intensity-modulated

signal change dI for sensitive detection. As shown by the blue curve in Fig. 5.13a, our experimental FOM* reaches a maximum value of 146 at a wavelength λ of 700.6 nm, slightly detuned from the interference valley wavelength of 705.1 nm. This observed FOM* value is higher than that achieved in state-of-the-art plasmonic perfect absorber sensors (87 at 1.7 μm [90]) and gold nanorod sensors (24 at 850 nm [91]). In addition, our planar single-layer interferometer design is simpler and more easily mass-produced than plasmonic absorbers, which consist of multiple functional layers and rely on reflection measurements [90]. The straightforward transmission geometry of our platform also simplifies the optical design and facilitates system miniaturization. It should be noted that the operational design wavelength of intensity-based detection scheme must be carefully tailored to match the incident wavelength, which can be accomplished for this platform by appropriately adjusting R. From Eq. 5.2, the relation between the interference valley wavelength λ_v and R can be described as:

$$\frac{\Delta\lambda_v}{\Delta R} = \frac{\lambda_v}{R} = c, \tag{5.6}$$

where $\Delta\lambda_v$ and ΔR are the changes in λ_v and R, respectively, and c is a constant determined by n_{spp} and φ_0. This equation constitutes a simple design rule, which we can easily use to tune λ_d by properly varying R. In Fig. 5.13b, we measured the transmission spectra for a series of interferometers with gradually increasing R from 4 to 4.4 μm. The corresponding operating wavelength clearly red-shifts with the increase in R and is plotted in Fig. 5.13c. The slope of the linear fit to the data points gives $\Delta\lambda_d / \Delta R$ = 0.15 nm/nm, in good agreement with λ_d/R of 0.16 nm/nm and verifying the proposed design rule.

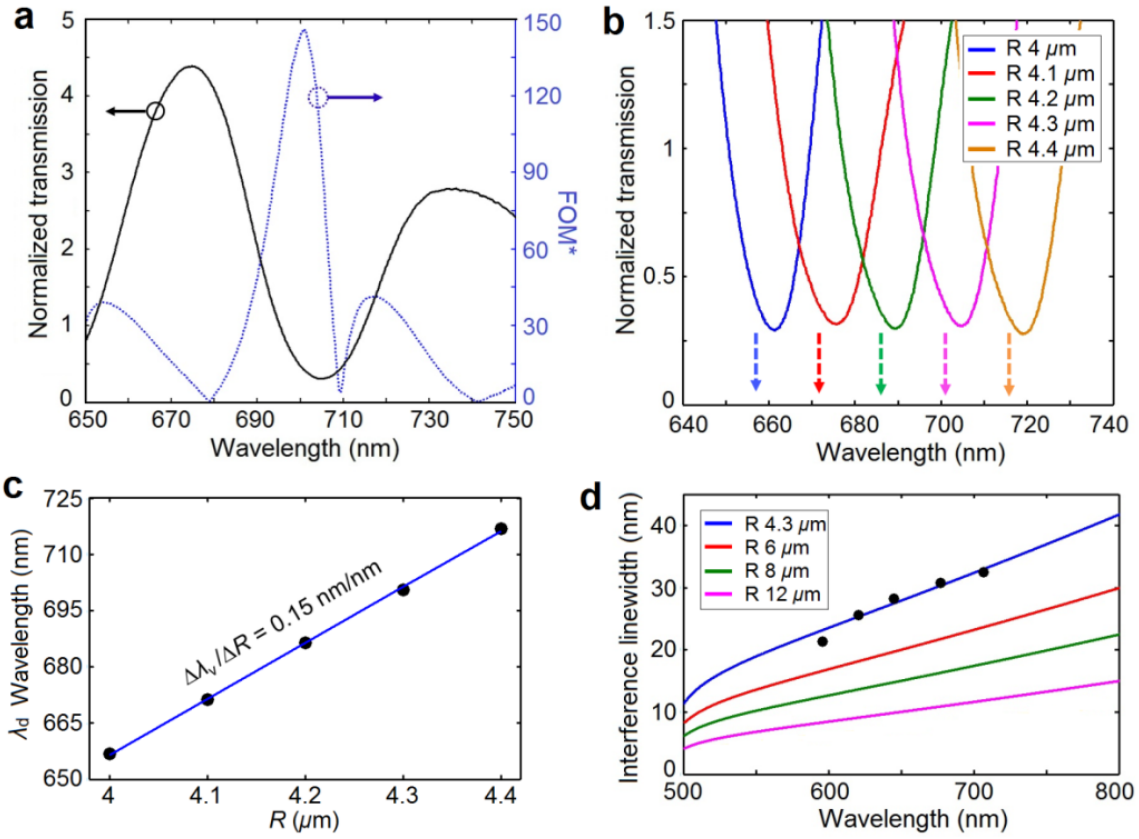

Fig. 5.13. Low-background interferometric sensing. (a) Experimental FOM* as a function of wavelength (blue dotted curve). Values of FOM* were derived using experimental spectra in water and 12% glycerol-water mixture to calculate dI/I_0 at each wavelength. The measured refractive index difference of 0.0177 was used in the denominator to calculate FOM*. The black solid curve represents the transmission spectrum of interferometers in water. (b) Normalized spectra of interferometers with tailored R of 4, 4.1, 4.2, 4.3, and 4.4 μm. The sensor operational wavelengths of 656.8, 671.3, 686.4, 700.6, and 716.8 nm (colored dashed arrows) are slightly detuned from their interference valley wavelengths. (c) The black dots represent the sensor operational wavelengths at different R. The blue line is the linear fit to the data points. (d) The solid curves show the calculated interference linewidths for interferometers with R of 4.3, 6, 8, and 12 μm. The black dots are experimental linewidths of interferometers with R of 4.3 μm, extracted from Fig. 5.6.

From the discussion above, one can see that similar to plasmonic perfect absorber sensors, the key issue in designing this interferometric sensor is to achieve near-perfect light suppression through destructive SPP-light interference. This can be realized under

two conditions. First, all geometric parameters of the interferometers need to be carefully designed to balance the intensities of SPPs and directly transmitted light near the sensor operating wavelength. Second, perfectly collimated illumination is required to eliminate additional SPP-light phase lag caused by different incident angles. While the first condition can be fulfilled through numerical simulations and fine-tuning of the structure geometry during fabrication, the microscope-based optical setup used in this work has a 3^{o} light divergence. A laser source and related collimating optics are being set up for better light collimation and to further optimize this intensity-based detection scheme. In addition to achieve perfect light cancellation, another way to optimize the sensor performance is to narrow the interference linewidth and thus to increase the values of dI/dn. As suggested by Eq. 5.3, this can be realized by increasing the SPP path length R. The curves in Fig. 5.13d show analytically calculated interference linewidths for R values of 4.3, 6, 8, and 12 μm, respectively. The interference linewidths clearly decrease with increasing R. The black dots represent extracted experimental linewidths for interferometers with R of 4.3 μm in Fig. 5.6, which exhibit close agreement with the analytical results and confirm the proposed analytical model. The increasing SPP loss associated with larger R can be easily compensated by fabricating a greater number of circular grooves to increase the generated SPP power. Note that while this method is not suitable for broadband spectral sensing as discussed in Fig. 5.8, it does not strongly affect single-wavelength intensity-based detection. As a result, rational design of R and the groove number should lead to further improvement in the sensing FOM* and corresponding sensor performance of this interferometric platform. Since this intensity-

based detection can be performed simply using a single-wavelength light source and a photodetector in a straightforward transmission geometry, it has the potential to significantly reduce the instrumentation cost of the biosensing device. Furthermore, a CCD camera can be integrated into this sensing platform for simultaneously monitoring of the light transmission from multiple sensor elements, making possible real-time highly-multiplexed detection. Another unique advantage of this sensor design is the minimal crosstalk between sensing pixels, which is especially useful to increase the sensor packing density for high-throughput detection. Here, the crosstalk between sensing pixels in our sensor array is minimal for two reasons. First, the circular grooves serve as both efficient SPP couplers and Bragg mirrors to block SPPs from adjacent sensing pixels. Second, the circular structure design ensures SPPs propagate radially towards adjacent structures. This allows only a very limited portion of SPPs propagate towards the hole locations of surrounding sensors and lead to unwanted cross-talk. To verify this hypothesis, we measured the spectra of sensor arrays with increasing sensor-to-sensor distance L from 12.5 to 20 μm (see Fig. 5.14). There is no obvious difference between collected spectra, demonstrating the minimal crosstalk between sensing pixels. This unique feature is useful for high-throughput multiplexed sensing as sensors can be more densely packed on the chip.

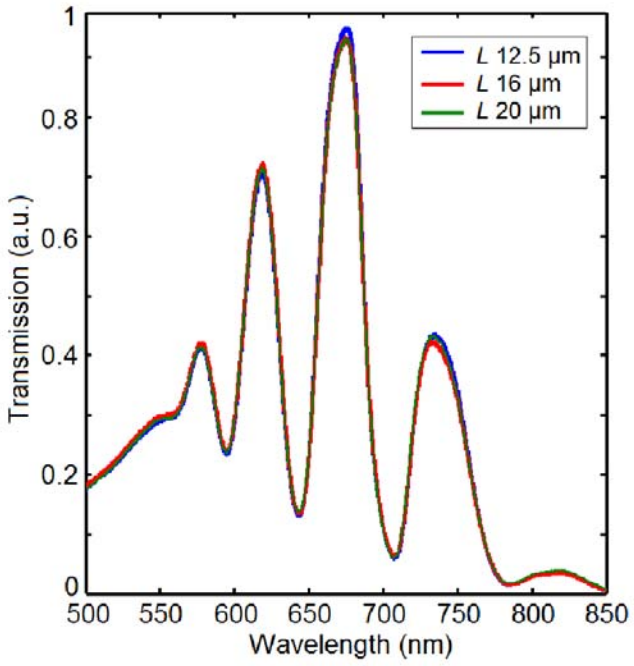

Fig. 5.14. The transmission spectra for sensor arrays with different sensor-to-sensor distances.

We now show the proof-of-principle imaging experiment using this novel sensing method. Filtered white light centered at 655 nm was transmitted through the 144 interferometers (Fig. 5.15a) and collected simultaneously using an X10 microscope objective and imaged onto a CCD camera. While 144 sensors were monitored in this proof-of-concept experiment, the current experimental setup can monitor up to 4000 sensors simultaneously, providing enough throughput for most biosensing applications. Fig. 5.15b shows the changes in sensor outputs of 144 sensors as the refractive index of the liquid was increased. The sensor resolution in this preliminary study was calculated to be around 1×10^{-5} RIU, among the best reported for intensity-modulated nanoplasmonic sensors [11,12,29,31]. Moreover, as seen by the shaded region in Fig. 5.15c, the FOM* of

this sensor at 655 nm is around 35, which is four times smaller than the maximum value achievable at 700.6 nm (see dotted blue line in Fig. 5.15c). In future work along this research direction, we will employ a highly stable single-wavelength laser source at the optimized working wavelength (700.6 nm in this experiment), instead of a filtered halogen lamp, together with effective referencing methods to further increase the sensor sensitivity and minimize effects of light intensity fluctuations. Note that, as shown in Fig. 5.13b, this optimized operating wavelength can be freely controlled by appropriately adjusting R to match the incident laser wavelength. Interferometric sensors with larger R values and more circular nanogrooves will be fabricated and tested for further sensitivity improvement. With structural optimization and performance improvement, the sensitivity and associated sensor detection limit of the proposed nanoplasmonic sensor platform is expected to improve by at least a factor of four to 2.5×10^{-6} RIU. This will compare favorably with or exceed that of commercial SPR imagers, but is based on a two orders of magnitude smaller sensor footprint of 10×10 μm^2. With the demonstrated superior sensing performance and possible further improvement, this sensor platform would lead to revolutionary advances in numerous high-throughput sensing applications.

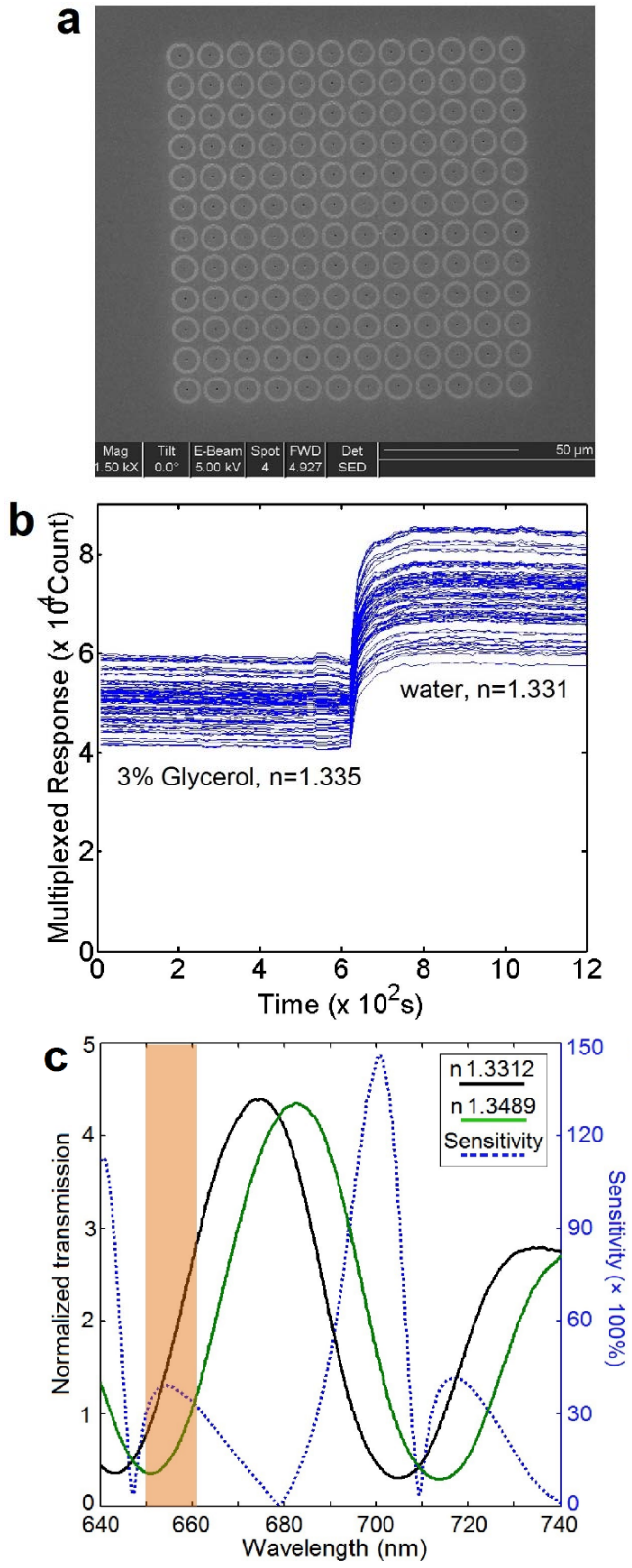
a
Mag 1.50 kX
Tilt 0.0°
E-Beam 5.00 kV
Spot 4
FWD 4.927
Det SED
50 µm
b
Multiplexed Response (x 10^4 Count)
Time (x 10^2 s)
water, n=1.331
3% Glycerol, n=1.335
c
Normalized transmission
Sensitivity (× 100%)
Wavelength (nm)
n 1.3312
n 1.3489
Sensitivity

Fig. 5.15. (a) SEM image of the fabricated 12 × 12 sensor array. (b) The real-time sensor output monitored simultaneously from 144 sensor elements, demonstrating the dynamic multiplexed sensing capability of the proposed sensor platform. (c) The measured spectra for sensors in water (black curve, n = 1.3312) and 12% glycerol-water mixture (green curve, n = 1.3489). The dotted blue curve is the calculated sensitivity using $S = (dI/I_0)/dn$. The orange region indicates the linewidth of the incident light for CCD imaging experiment. By using a single-wavelength laser source at 700.6 nm, the sensitivity is expected to further increase by 4 times.

5.4 Summary

In summary, in this chapter we have further optimized the plamsonic interferometer design, which is suitable for both sensitive single-channel spectral sensing and high-throughput multiplexed imaging. Through careful and optimized design of the structural parameters, we have observed spectral interference fringes with high contrast, large amplitudes, and narrow linewidths, and achieved an enhanced spectral sensing resolution of 0.4 pg/mm^2 within a small (150 μm × 150 μm) sensing area. This demonstrated superior resolution and simple optical geometry suggests exciting potential for low-cost portable biosensing devices, which would significantly impact point-of-care diagnostics and personal healthcare applications. The demonstrated sensor resolution compares favourably with state-of-the-art commercial SPR systems. In addition, we demonstrated sensitive multiplexed detection in imaging mode using a novel low-background interferometric sensing concept, and achieved a record-high FOM* value of 146. This surpasses previous plasmonic sensors and still holds potential for further improvement through the optimization of the device structure. In our proof-of-concept experiment, we have demonstrated multiplexed detection with a sensing resolution of 1 × 10^{-5} RIU, comparable to commercial SPR imagers. This demonstrated sensor platform may serve as

a promising tool for high-throughput applications in drug discovery, screening of novel therapies, proteomics, immunology, and basic biology research.

Chapter 6

Conclusions and future directions

In this chapter, we first summarize the results achieved in this dissertation and then propose future research directions.

6.1 Conclusions

This dissertation discusses design and fabrication of several plasmonic interferometer nanostructures for applications in sensitive biomolecular detection, and achieves superior sensing performance comparable to state-of-the-art commercial SPR systems but based on significantly simpler optical setup and smaller sensor footprint, showing great promise for miniaturized portable biomedical devices with massive multiplexing capacity.

In Chapter 3, we demonstrated, for the first time, a plasmonic interferometric biosensor, which exhibits a refractive index sensitivity over 3000 nm/RIU, 10 times better than previous nanoplasmonic sensors. This sensor platform also exhibits a record-high sensing figure of merit exceeding 200, demonstrating the promise of plasmonic interferometric sensing technique.

High-throughput sensing has important application in various fields. In Chapter 4, the proposed plasmonic interferometers were further designed and fabricated in a high-density array format to extend its use for dynamic multiplexed detection. Instead of the spectral sensing method employed in Chapter 3, narrow-band illumination and CCD imaging were used in this modified sensor array platform for imaging-based multiplexed detection. A novel self-referencing method was also proposed to improve the sensing

performance.

In Chapter 2 and 3, we have demonstrated the feasibility of plasmonic interferometric sensor platform for single-channel sensing and imaging-based multiplexing, respectively. Chapter 5 discussed the further optimization of plasmonic interferometers for both applications. Through novel interferometer structure design and optimization, we have demonstrate in this chapter an enhanced single-channel sensor resolution of 0.4 pg/mm^2, comparing favorably with state-of-the-art commercial SPR systems (0.1 pg/mm^2). The simple collinear transmission setup and two orders of magnitude smaller sensing area are important advantages and open up opportunities to greatly decrease the size and cost of SPR systems without compromising the performance. We also proposed in this chapter a novel low-background intensity-based sensing method. Using this approach, we have demonstrated dynamic, 144-channel, multiplexed sensing with a resolution of 1×10^{-5} RIU. While the sensor resolution we demonstrated is comparable to commercial SPR imagers, the achieved 100 μm^2 sensor footprint is two orders of magnitude smaller than commercial systems, significantly increasing the sensor throughput and also facilitating the probe of nanovolumes and single-cell detection.

6.2 Future directions

Further performance improvement. While the demonstrated sensor resolution for both single-channel and multiplexed sensing are comparable to commercial SPR and SPRi systems, significant improvements in sensor performance are still possible. For example, the use of ultrasmooth metal films to decrease SPP propagation loss or the fabrication of

a larger sensor array to increase the light transmission can both help to improve the spectral signal-to-noise ratio and the resulting sensing resolution. For imaging-based multiplexing, instead of a filtered halogen lamp, a highly-tunable laser source, together with effective referencing methods, can be used to further increase the sensor sensitivity and minimize effects of light intensity fluctuations. Circular interferometers with larger radii and more circular nanogrooves can also be fabricated and tested to decrease the interference linewidth for further sensitivity improvement. These approaches for structure and system optimization using this platform should lead to improved sensitivity and associated sensing resolution.

Sensing in complex samples. To facilitate the application in real biomedical diagnostics, this demonstrated plasmonic sensor platform needs to be able to detect analytes in complex biological samples such as blood, serum, urine, etc. To achieve this goal, the next-step would be to optimize the surface modification protocols to maintain receptor stability and minimize non-specific bindings in a complex solution. It is also important to include a reference channel, which lacks the receptor coating and thus only responds to bulk changes or environmental factors such as temperature and mechanical vibration. Signal from the reference sensors will then be subtracted from those on the functional sensors to yield exclusive target molecule binding signals.

Sensor miniaturization. One unique advantage of nanoplasmonic sensors with respect to commercially available systems is their low-cost producability and potential for miniaturization. For example, replacing the spectrometer and white light source with a simple CMOS detector and a LED light source will significantly decrease the cost and

size of the system, although tradeoffs must be made between spatial resolution and performance degradation. Combining nanoplamsonic sensor chip with smart phone technology is another interesting research direction that is worth pursuing. Finally, to commercialize the developed sensor system, we also need to package the sensor system, develop a user-friendly software and hardware interface, and automate the instrument operation and sample handling.

References:

[1] D. G. Buerk, "Biosensor: Theory and application", Technomic Publishing, 1993, Lancaster, PA.

[2] J. Homola, "Surface plasmon resonance based sensors", Springer, 2006, New York.

[3] X. Fan, I. M. White, S. I. Shopova, H. Zhu, J. D. Suter, and Y. Sun, "Sensitive optical biosensors for unlabeled targets: A review," Anal. Chemica. Acta. 620, 8-26 (2008).

[4] J. Homola, "Surface plasmon resonance sensors for detection of chemical and biological species," Chem. Rev. 108, 462-493 (2008).

[5] M. A. Cooper, "Optical biosensors in drug discovery," Nature Rev., 1, 515-528 (2002).

[6] J. Comley, "Progress in the implementation of label-free detection, part 2: binding analysis assays," Drug Discovery World, Fall Edition, 28-49 (2008).

[7] A. De Leebeeck, L. K. S. Kumar, V. de Lange, D. Sinton, R. Gordon, and A. G. Brolo, "On-chip surface-based detection with nanohole arrays," Anal. Chem. 79, 4094-4100 (2007).

[8] A. Cattoni, P. Ghenuche, A. M. Haghiri-Gosnet, D. Decanini, J. Chen, J. L. Pelouard, and S. Collin, "$\lambda^3/1000$ plasmonic nanocavities for biosensing fabricated by soft UV nanoimprint lithography," Nano Lett. 11, 3557-3563 (2011).

[9] A. G. Brolo, "Plasmonics for future biosensors," Nature Photon. 6, 709-713 (2012).

[10] N. C. Lindquist, A. Lesuffleur, H. Im, and S. H. Oh, "Sub-micron resolution surface plasmon resonance imaging enabled by nanohole arrays with surrounding Bragg mirrors for enhanced sensitivity and isolation," Lab Chip 9, 382-387 (2009).

[11] J. C. Yang, J. Ji, J. M. Hogle, and D. N. Larson, "Multiplexed plasmonic sensing based on small-dimension nanohole arrays and intensity interrogation," Biosens. Bioelectron. 24, 2334-2338 (2009).

[12] J.C. Yang, J. Ji, J.M. Hogle, and D.N. Larson, "Metallic nanohole arrays on fluoropolymer substrates as small label-free real-time bioprobes," Nano Lett. 8, 2718-2724 (2008).

[13] A. Lesuffleur, H. Im, N.C. Lindquist, K.S. Lim, and S.H. Oh, "Laser-illuminated nanohole arrays for multiplex plasmonic microarray sensing," Opt. Express 16, 219-224 (2008).

[14] C. Genet, and T. W. Ebbesen, "Light in tiny holes," Nature 445, 39-46 (2007).

[15] J. A. Schuller, E. S. Barnard, W. Cai, Y. Jun, J .S. White, and M. L. Brongersma, "Plasmonics for extreme light concentration and manipulation," Nat. Mater. 9, 193-204 (2010).

[16] S. A. Maier, Plasmonics: Fundamental and applications, 2007, Springer, New York.

[17] M. E. Stewart, C. R. Anderton, L. B. Thompson, J. Maria, S. K. Gray, J. A. Rogers, and R. G. Nuzzo, "Nanostructured plasmonic sensors," Chem. Rev. 108, 494-521 (2008).

[18] J. N. Anker, W. P. Hall, O. Lyandres, N. C. Shah, J. Zhao, and R. P. Van Duyne, "Biosensing with plasmonic nanosensors," Nat. Mater. 7, 442-453 (2008).

[19] K. M. Mayer and J. H. Hafner, "Localized surface plasmon resonance sensors," Chem. Rev. 111, 3828-3857 (2011).

[20] M. Piliarik and J. Homola, "Surface plasmon resonance (SPR) sensors: approaching their limits?," Opt. Express 17, 16505-16517 (2009).

[21] C.T. Campbell and G. Kim, "SPR microscopy and its applications to high-throughput analyses of biomolecular binding events and their kinetics," Biomaterials 28, 2380-2392 (2007).

[22] D. Boecker, A. Zybin, V. Horvatic, C. Grunwald, and K. Niemax, "Differential surface plasmon resonance imaging for high-throughput bioanalyses," Anal. Chem. 79, 702-709 (2007).

[23] G. Spoto and M. Minunni, "Surface plasmon resonance imaging: what next?," Phys. Chem. Lett. 3, 2682-2691 (2012).

[24] N. Blow, "Proteins and proteomics: life on the surface," Nature Methods 6, 389-393 (2009).

[25] J. S. Shumaker-Parry and C. T. Campbell, "Quantitative methods for spatially resolved

adsorption/desorption measurements in real time by surface plasmon resonance microscopy," Anal. Chem. 76, 907-917 (2004).

[26] http://www.gwcinstruments.com

[27] http://www.horiba.com/us/en

[28] http://www.lumera.com

[29] H. Im, A. Lesuffleur, N.C. Lindquist, and S.H. Oh, "Plasmonic nanoholes in a multichannel microarray format for parallel kinetic assays and differential sensing," Anal. Chem. 81, 2854-2859 (2009).

[30] T. Y. Chang, M. Huang, A. A. Yanik, H. Y. Tsai, P. Shi, S. Aksu, M. F. Yanik, and H. Altug, "Large-scale plasmonic microarrays for label-free high-throughput screening," Lab Chip 11, 3596-3602 (2011).

[31] C. Escobedo, S. Vincent, A. I. K. Choudhury, J. Campbell, A. G. Brolo, D. Sinton, and R. Gordon, "Integrated nanohole array surface plasmon resonance sensing device using a dual-wavelength source," J. Micromech. Microeng. 21, 115001 (2011).

[32] M. Piliarik, H. Vaisocherova, and J. Homola, "A new surface plasmon resonance sensor for high-throughput screening applications," Biosens. & Bioelectron. 20, 2104-2110 (2005).

[33] A. A. Yanik, A. E. Cetin, M. Huang, A. Artar, S. H. Mousavi, A. Khanikaev, J. H. Connor, G. Shvets, and H. Altug, “Seeing protein monolayers with naked eye through plasmonic Fano resonances,” Proc. Natl. Acad. Sci. USA 108, 11784-11789 (2011).

[34] Y. Gao, Q. Gan, Z. Xin, X. Cheng, and F. J. Bartoli, "Plasmonic Mach-Zehnder Interferometer for Ultrasensitive On-Chip Biosensing," ACS Nano 5, 9836-9844 (2011).

[35] Y. Gao, Z. Xin, Q. Gan, X. Cheng, and F.J. Bartoli, "Plasmonic interferometers for label-free multiplexed sensing," Opt. Express 21, 5859-5871 (2013).

[36] Y. Gao, Z. Xin, B. Zeng, Q. Gan, X. Cheng, and F. J. Bartoli, "Plasmonic interferometric sensor arrays for high-performance label-free biomolecular detection," Lab Chip 13, 4755-4764 (2013).

[37] P. Hariharan, "Optical interferometry," Academic Press, 2003, Amsterdam.

[38] A. Kussrow, C. S. Enders, and D. J. Bornhop, "Interferometric methods for label-free molecular interaction studies," Anal. Chem. 84, 779-792 (2012).

[39] http://h2physics.org/?cat=48

[40] A. Densmore, M. Vachon, D. X. Xu, S. Janz, R. Ma, Y. H. Li, G. Lopinski, A. Delage, J. Lapointe, C. C. Luebbert, Q. Y. Liu, P. Cheben, J. H. Schmid, Opt. Lett. 34, 3598–3600 (2009).

[41] Y. Huang, H. P. Ho, S. K. Kong, and A. V. Kabashin, "Phase-sensitive surface plasmon resonance biosensors: methodology, instrumentation and applications," Ann. Phys. 524, 637–662 (2012).

[42] H. F. Schouten, N. Kuzmin, G. Dubois, T. D. Visser, G. Gbur, P. F. A. Alkemade, H. Blok, G. W. ’t Hooft, D. Lenstra, and E. R. Eliel,"Plasmon-assisted two-slit transmission: Young's experiment revisited," Phys. Rev. Lett. 94, 053901 (2005).

[43] V. V. Temnov, U. Woggon, J. Dintinger, E. Devaux, and T. W. Ebbesen, "Surface plasmon interferometry: measuring group velocity of surface plasmons," Opt. Lett. 32, 1235-1237 (2007).

[44] Q. Gan, Y. Gao, Q. Wang, L. Zhu, and F. J. Bartoli, "Surface plasmon waves generated by nanogrooves through spectral interference," Phys. Rev. B 81, 085443 (2010).

[45] N. Liu, T. Weiss, M. Mesch, L. Langguth, U. Eigenthaler, M. Hirscher, C. Sonnichsen, and H. Giessen, "Planar metamaterial analogue of electromagnetically induced transparency for plasmonic sensing," Nano Lett. 10, 1103-1107 (2010).

[45] N. Verellen, P. Van Dorpe, C. J. Huang, K. Lodewijks, G. A. E. Vandenbosch, L. Lagae, and V. V. Moshchalkov, "Plasmon line shaping using nanocrosses for high sensitivity localized surface plasmon resonance sensing," Nano Lett. 11, 391-397 (2011).

[46] S. Zhang, K. Bao, N. J. Halas, H. Xu, and P. Nordlander, "Substrate-induced Fano resonances of a plasmonic nanocube: a Route to increased-sensitivity localized surface plasmon resonance sensors revealed," Nano Lett. 11, 1657-1663 (2011).

[47] B. Gallinet, and O. J. F. Martin, "Influence of electromagnetic interactions on the line Shape of plasmonic Fano resonances," ACS Nano 5, 8999-9008 (2011).

[48] M. Rahmani, D. Y. Lei, V. Giannini, B. Lukiyanchuk, M. Ranjbar, T. Y. F. Liew, M. Hong, and S. A. Maier, "Subgroup decomposition of plasmonic resonances in hybrid Oligomers: modeling the resonance lineshape," Nano Lett. 12, 2101-2106 (2012).

[49] S. H. Lee, T. W. Johnson, N. C. Lindquist, H. Im, D. J. Norris, and S-H. Oh, "Linewidth-optimized extraordinary optical transmission in water with template-stripped metallic nanohole arrays," Adv. Func. Mater. 22, 4439-4446 (2012).

[50] P. Lalanne, J. P. Hugonin, "Interaction between optical nano-Objects at metallo-dielectric interfaces," Nat. Phys. 2, 551-556 (2006).

[51] G. Gay, O. Alloschery,B. Viaris De Lesegno, C. O'. Dwyer, J. Weiner,H. J. Lezec, "The optical response of nanostructured surfaces and the composite diffracted evanescent wave model," Nat. Phys. 2, 262-267 (2006).

[52] H. E. Bennett, R. L. Peck, D. K. Burge, J. M. Bennett, "Formation and growth of tarnish on evaporated silver films," J. Appl. Phys. 40, 3351-3360 (1969).

[53] J. M. Bennett, J. L. Stanford, E. J. Ashley, "Optical constants of silver sulfide tarnish films," J. Opt. Soc. Am. 60, 224-231 (1970).

[54] J. Tominaga, "The application of silver oxide thin films to plasmon photonic devices," J. Phys.: Condens. Matter 15, R1101-R1122 (2003).

[55] M. H. Lee, H. Gao, T. W. Odom, "Refractive index sensing using quasi one-dimentional nanoslit arrays," Nano lett. 9, 2584-2588 (2009).

[56] J. Henzie, M. H. Lee, T. W. Odom, "Multiscale patterning of plasmonic metamaterials," Nat. Nanotech. 2, 549-554 (2007).

[57] M. E. Stewart, N. H. Mack, V. Malyarchuk, J. A. N. T. Soares, T. W. Lee, S. K. Gray, R. G. Nuzzo, J. A. Rogers, "Quantitative multispectral biosensing and 1D imaging using quasi-3D plasmonic crystals," Proc. Natl. Acad. Sci. U.S.A. 103, 17143-17148 (2006).

[58] A. M. Otte, B. Sepulveda, W. Ni, J. P. Juste, L. M. Liz-Marzan, L. M. Lechuga, "Identification of the optimal spectral region for plasmonic and nanoplasmonic sensing," ACS Nano 4, 349-357 (2010).

[59] L. J. Sherry, S. H. Chang, G. C. Schatz, R. P. Van Duyne, B. J. Wiley, Y. Xia, "Localized surface plasmon resonance spectroscopy of single silver nanocubes," Nano Lett. 5, 2034-2038 (2005).

[60] E. M. Hicks, X. Zhang, S. Zou, O. Lyandres, K. G. Spears, G. C. Schatz, R. P. Van Duyne, "Plasmonic properties of film over nanowell surfaces fabricated by nanosphere lithography," J. Phys. Chem. B 109, 22351-22358 (2005).

[61] K. A. Tetz, L. Pang, Y. Fainman, "High-resolution surface plasmon resonance sensor based on linewidth-optimized nanohole array transmittance," Opt. Lett. 31, 1528-1530 (2006).

[62] P. Nagpal, N. C. Lindquist, S. Oh, D. J. Norris, "Ultrasmooth patterned metals for plasmonics and metamaterials," Science 325, 594-597 (2009).

[63] X. Zhu, Y. Zhang, J. Zhang, J. Xu, Y. Ma, Z. Li, D. Yu, "Ultrafine and smooth full metal nanostructures for plasmonics. Adv. Mater. 22, 4345-4349 (2010).

[64] H. Im, S. H. Lee, N. J. Wittenberg, T. W. Johnson, N. C. Lindquist, N. Prashant, D. J. Norris, S-H Oh, Template-stripped smooth Ag nanohole arrays with silica shells for surface plasmon resonance biosensing," ACS Nano 5, 6244-6253 (2011).

[65] O. Vazquez-Mena, T. Sannomiya, L. G. Villanueva, J. Voros, J. Brugger, "Metallic nanodot arrays by stencil lithography for plasmonic biosensing applications," ACS Nano 5, 844-853 (2011).

[66] T. Sannomiya, P. K. Sahoo, D. I. Solak, H. H. Hafner, C. Grieshaber, D. Voros, "Biosensing by densely packed and optically coupled plasmonic particle arrays," Small 5, 1889-1896 (2009).

[67] A. D. Leebeeck, L. K. Swaroop Kumar, V. D. Lange, D. Sinton, R. Gordon, A. G. Brolo, "On-chip surface-based detection with nanohole arrays," Anal. Chem. 79, 4094-4100 (2007).

[68] G. Raschke, S. Kowarik, T. Franzl, C. Sönnichsen, T. A. Klar, J. Feldmann, A. Nichtl, K. Kurizinger, "Biomolecular recognition based on single gold nanoparticle light scattering," Nano Lett. 3, 935-938 (2003).

[69] L. S. Jung, C. T. Campbell, T. M. Chinowsky, M. N. Mar, S. S. Yee, "Quantitative interpretation of the response of surface plasmon resonance sensors to adsorbed films," Langmuir 14, 5636-5648 (1998).

[70] L. Haussling, H. Ringsdorf, F. J. Schmitt, W. Knoll, "Biotin-functionalized self-assembled monolayers on gold: surface plasmon optical studies of specific recognition reactions," Langmuir 7, 1837-1840 (1991).

[71] A. A. Kolomenskii, P. D. Gershon, H. A. Schuessler, "Sensitivity and detection limit of concentration and adsorption measurements by laser-induced surface-plasmon resonance," Appl. Opt. 36, 6539-6547 (1997).

[72] M. Piliarik, H. Vaisocherova, and J. Homola, “A new surface plamson resonance sensor for high-throughput screening applications,” Biosens. Bioelectron. 20, 2104-2110 (2005).

[73] A. B. Dahlin, S. Chen, M. P. Jonsson, L. Gunnarsson, M. Käll, and F. Höök, "High-resolution microspectroscopy of plasmonic nanostructures for miniaturized biosensing," Anal. Chem. 81, 6572-6580 (2009).

[74] A. B. Dahlin, J. O. Tegenfeldt, and F. Höök, "Improving the instrumental resolution of sensors based on localized surface plasmon resonance," Anal. Chem. 78, 4416-4423 (2006).

[75] J. Ruemmele, W. P. Hall, L. K. Ruvuna, and R. P. Van Duyne, "A localized surface plasmon resonance imaging instrument for multiplexed biosensing," Anal. Chem. 85, 4560-4566 (2013).

[76] T. Endo, K. Kerman, N. Nagatani, H. M. Hiepa, D. K. Kim, Y. Yonezawa, K. Nakano, and E. Tamiya, "Multiple label-free detection of antigen−antibody reaction using localized surface plasmon resonance-based core−shell structured nanoparticle layer nanochip," Anal. Chem. 78, 6465-6475 (2006).

[77] J. Ji, G. O'Connel, D. J. D. Carter, and D. N. Larson, "High-throughput nanohole array based system to monitor multiple binding events in real time," Anal. Chem. 80, 2491-2498 (2008).

[78] J. Bravo-Abad, L. Martin-Moreno, and F. J. Garcia-Vidal, "Transmission properties of a single metallic slit: From the subwavelength regime to the geometrical-optics limit," Phys. Rev. E 69, 026601 (2004).

[79] J. Feng, V. S. Siu, A. Roelke, V. Mehta, S. Y. Rhieu, G. T. R. Palmore, and D. Pacifici, "Nanoscale plasmonic interferometers for multispectral, high-throughput biochemical sensing," Nano Lett. 12, 602-609 (2012).

[80] X. Li, Q. Tan, B. Bai, and G. Jin, "Non-spectroscopic refractometric nanosensor based on a tilted slit-groove plasmonic interferometer," Opt. Express 19, 20691-20703 (2011).

[81] O. Yavas and C. Kocabas, "Plasmon interferometers for high-throughput sensing," Opt. Lett. 37, 3396-3398 (2012).

[82] K-L. Lee, P-W. Chen, S-H. Wu, J-B. Huang, S-Y. Yang, and P-K. Wei, "Enhancing surface plasmon detection using template-stripped gold nanoslit arrays on plastic films," ACS Nano 6, 2931-2939 (2012).

[83] P. Lalanne, J. P. Hugonin, and J. C. Rodier, “Theory of surface plasmon generation at nanoslit apertures,” Phys. Rev. Lett. 95, 263902 (2005).

[84] J. S. Q. Liu, R. A. Pala, F. Afshinmanesh, W. Cai, and M. L. Brongersma, "A submicron plasmonic dichroic splitter," Nat. Comm. 2, 525 (2011).

[85] M. U. Gonzalez, J. C. Weeber, A. L. Baudrion, A. Dereux, A. L. Stepanov, J. R. Krenn, E. Devaux, and T. W. Ebbesen, "Design, near-field characterization, and modeling of 450 surface-plasmon Bragg mirrors," Phys. Rev. B 73, 155416 (2006).

[86] J. A. Sanchez-Gil and A. A. Maradudin, "Surface-plasmon polariton scattering from a finite array of nanogrooves/ridges: Efficient mirrors," Appl. Phys. Lett. 86, 251106 (2005).

[87] N. C. Lindquist, T. W. Johnson, D. J. Norris, and S. H. Oh, “Monolithic integration of continuously tunable plasmonic nanostructures,” Nano Lett. 11, 3526-3530 (2011).

[88] Z. Liu, J. M. Steele, W. Srituravanich, Y. Pikus, C. Sun, and X. Zhang, "Focusing surface plasmons with a plasmonic lens,"Nano Lett. 5, 1726-1729 (2005).

[89] C. Valsecchi, and A. G. Brolo, "Periodic metallic nanostructures as plasmonic chemical sensors," langmuir, 29, 5638-5649 (2013).

[90] N. Liu, M. Mesch, T. Weiss, M. Hentschel, and H. Giessen, "Infrared Perfect Absorber and Its Application As Plasmonic Sensor," Nano Lett. 10, 2342-2348 (2010).

[91] J. Becker, A. Trugler, A. Jakab, U. Hohenester, and C. Sonnichsen, "The optimal aspect ratio of gold nanorods for plasmonic bio-sensing," Plasmonics, 5, 161-167 (2010).

[92] T. Thio, K. M. Pellerin, R. A. Linke, H. J. Lezec, and T. W. Ebbesen, "Enhanced light transmission through a single subwavelength aperture," Opt. Lett. 26, 1972-1974 (2001).

[93] E. Laux, C. Genet, T. Skauli, and T. W. Ebbesen, "Plasmonic photon sorters for spectral and polarimetric imaging," Nat. Photon. 2, 161-164 (2008).

[94] X. Wu, J. Zhang, J. Chen, C. Zhao, and Q. Gong, "Refractive index sensor based on surface-plasmon interference," Opt. Lett. 34, 392-394 (2009).

[95] G. Gay, O. Alloschery, B. V. de Lesegno, J. Weiner, and H. J. Lezec, "Surface wave generation and propagation on metallic subwavelength structures measured by far-field interferometry," Phys. Rev. Lett. 96, 213901 (2006).

[96] H. Im, J. N. Sutherland, J. A. Maynard, and S-H. Oh, "Nanohole-based surface plasmon resonance instruments with improved spectral resolution quantify a broad range of antibody-ligand binding kinetics," Anal. Chem. 84, 1941-1947 (2012).

Yongkang Gao

Rm219, 7 ASA Drive, Bethlehem, PA 18015
Phone: 610-573-7175 | E-mail: yog208@lehigh.edu

Research Interests

Nanophotonic structures and devices, Plasmonics, Biophotonics, Optoelectronics.

Education

Lehigh University, Bethlehem, PA, USA
Ph.D. Electrical Engineering Jan. 2014
• Concentration in design, modeling, fabrication and characterization of novel plasmonic nanostructures, with applications in miniaturized biosensor chip, solar energy harvesting, and color filtering in CMOS image sensors.
• GPA: 3.9/4.0
• Rossin Doctoral Fellow (2009-2010); Lehigh University Dean's Scholarship (2008-2009).

Beijing University of Posts and Telecommunications (BUPT), Beijing, China
B.S. Optical Communication Jul. 2008
• GPA: 86.63/100 (Rank: **2nd/60**)
• First-Class Scholarship (top **5%**), three times (2005, 2006, 2007); Excellent Student Award, three times (2005, 2006, 2007); Excellent Student Leader Award (2007).

Professional Experiences

Lehigh University, Bethlehem, PA, USA Sep. 2008 – present
Research Assistant
• Optical biosensor chip for ultrasensitive biomedical sensing
  – Designed and fabricated plasmonic nanosensor chip using focused ion beam and photolithography with demonstrated superior detection sensitivity.
  – Built and aligned the laser and optical spectroscopy and imaging systems and developed algorithms for automatic data processing.
  – Performed thin film deposition (PECVD, ALD) and characterization (ellipsometry, SEM, AFM) for sensor surface coating.
• Nanopatterned metal films for color filtering
  – Successfully conducted modeling (Rsoft, Lumerical) and fabrication of novel surface plasmon color filters for CMOS image sensors and display application.
  – Proposed a unique concept to control the transparency of the metal film by tuning the light polarization, useful for transparent display.

Skills and Expertise

Lab Skills: Focused ion beam lithography (FIB), Photolithography, Scanning electron microscopy (SEM), E-beam deposition, Atomic force microscopy (AFM), Atomic layer deposition (ALD), Ellipsometry, PECVD, Optical microscopy, Spectroscopy and imaging characterization, Microfluidics fabrication, Optical system design, Nanophotonic device design and fabrication.

Numerical Tools: Matlab, Rsoft, Lumerical (based on FDTD/RCWA methods).

Journal Publications

[10] Y. Gao, Z. Xin, B. Zeng, Q. Gan, X. Cheng, and F. J. Bartoli, “Plasmonic interferometric sensor arrays for high-performance label-free biomolecular detection”, Lab Chip, Cover Article, 13, 4755, 2013.
[9] B. Zeng, Y. Gao, and F. J. Bartoli, “Ultrathin nanopatterned metals for subtractive plasmonic color filtering”, Scientific Report, 3, 2840, 2013.
[8] X. Zeng, Y. Gao, H. Hu, D. Ji, Q. Gan, and F. J. Bartoli, “A metal-insulator-metal plasmonic Mach-Zehnder interferometer array for multiplexed sensing”, J. Appl. Phys., 113, 133102, 2013.
[7] Y. Gao, Z. Xin, Q. Gan, X. Cheng, and F. J. Bartoli, “Plasmonic interferometers for multiplexed label-free sensing”, Opt. Express, 21, 5859, 2013.
[6] Q. Gan, W. Bai, S. Jiang, Y. Gao, W. Li, W. Wu, and F. J. Bartoli, “Short-range surface plasmon polaritons for extraordinary low transmission through ultra-thin metal films with nanopatterns”, Plasmonics, 7, 47, 2013.
[5] Y. Gao, Q. Gan, and F. J. Bartoli, “Spatially selective plasmonic sensing using metallic nanoslit arrays”, IEEE JSTQE, 20, 6900306, 2013.
[4] Y. Gao, Z. Xin, Q. Gan, X. Cheng, and F. J. Bartoli, “Plasmonic Mach-Zehnder interferometer for ultrasensitive on-chip biosensing”, ACS Nano, 5, 9836, 2011.
[3] Q. Gan, Y. Gao, K. Wagner, D. Vezenov, Y. J. Ding, and F. J. Bartoli, “Experimental verification of the rainbow trapping effect in adiabatic plasmonic gratings”, Proc. Natl. Acad. Sci. U.S.A. (PNAS), 108, 5169, 2011.
[2] Q. Gan, Y. Gao, Q. Wang, L. Zhu, and F. J. Bartoli, “Observation of surface plasmon waves generated by nanogrooves through spectral interference”, Phys. Rev. B., 81, 085443, 2010.
[1] Q. Gan, Y. Gao, and F. J. Bartoli, “Vertical plasmonic Mach-Zehnder interferometer for ultra-sensitive optical sensing”, Opt. Express, 17, 20747, 2009.

Other Professional Activities

Current Professional Society Membership: Institute of Electrical and Electronics Engineers (IEEE) member (2009-2013), IEEE Photonics Society member (2009-2013), Sigma Xi member (2011-2013).

Journal Reviewer: Optics Express, Optics Letters, Applied Physics Letters, Journal of Applied physics, IEEE Photonics Journal, IEEE Photonics Technology Letters, Optics Communications, IEEE Transactions on Nanotechnology.